

cy.2

OCT 30 1979



INTEGRAL SOLUTION OF COMPRESSIBLE TURBULENT BOUNDARY LAYERS USING IMPROVED VELOCITY PROFILES

David L. Whitfield
ARO, Inc., a Sverdrup Corporation Company

PROPELLION WIND TUNNEL FACILITY
ARNOLD ENGINEERING DEVELOPMENT CENTER
AIR FORCE SYSTEMS COMMAND
ARNOLD AIR FORCE STATION, TENNESSEE 37389

December 1978

Final Report for Period March — November 1977

Approved for public release; distribution unlimited.

Property of U. S. Air Force
AEDC LIBRARY
F0030, A-0-003

Prepared for

ARNOLD ENGINEERING DEVELOPMENT CENTER/DOTR
ARNOLD AIR FORCE STATION, TENNESSEE 37389

NOTICES

When U. S. Government drawings, specifications, or other data are used for any purpose other than a definitely related Government procurement operation, the Government thereby incurs no responsibility nor any obligation whatsoever, and the fact that the Government may have formulated, furnished, or in any way supplied the said drawings, specifications, or other data, is not to be regarded by implication or otherwise, or in any manner licensing the holder or any other person or corporation, or conveying any rights or permission to manufacture, use, or sell any patented invention that may in any way be related thereto.

Qualified users may obtain copies of this report from the Defense Documentation Center.

References to named commercial products in this report are not to be considered in any sense as an indorsement of the product by the United States Air Force or the Government.

This report has been reviewed by the Information Office (OI) and is releasable to the National Technical Information Service (NTIS). At NTIS, it will be available to the general public, including foreign nations.

APPROVAL STATEMENT

This report has been reviewed and approved.

Elton R. Thompson
ELTON R. THOMPSON
Project Manager, Research Division
Directorate of Test Engineering

Approved for publication:

FOR THE COMMANDER

Robert W. Crossley
ROBERT W. CROSSLEY, Lt Colonel, USAF
Acting Director of Test Engineering
Deputy for Operations

UNCLASSIFIED

UNCLASSIFIED

20. ABSTRACT (Continued)

and Reynolds number based on momentum thickness, thus no new parameters not already occurring in the integral equations are introduced. The velocity-temperature relation is also an analytical expression that describes the total-temperature overshoot near the outer edge of turbulent adiabatic wall boundary layers with nonunity Prandtl number and recovery factor. The method is fast, easy to use, and shown to provide good agreement with experimental data. The resulting computer code is relatively small. A computer program listing that is applicable to the calculation of impermeable, adiabatic wall, turbulent boundary layers for Mach numbers up to three is included.

PREFACE

The work reported herein was conducted by the Arnold Engineering Development Center (AEDC), Air Force Systems Command (AFSC), by ARO, Inc., AEDC Division (a Sverdrup Corporation Company), operating contractor for the AEDC, AFSC, Arnold Air Force Station, Tennessee, under ARO Projects No. P33A-G4A and P32A-P2A. The Air Force project manager of this work was Elton R. Thompson, DOTR, AEDC.

The author acknowledges Tracy L. Donegan, Cooperative Engineering Student, University of Tennessee, Knoxville, Tennessee, for his assistance in this work.

CONTENTS

	<u>Page</u>
1.0 INTRODUCTION	7
2.0 ANALYSIS	
2.1 Derivation of the Integral Equations	9
2.2 Wall Shear Stress	13
2.3 Velocity Profile	14
2.4 Shear-Work Integral	16
2.5 Velocity-Temperature Relations	17
2.6 Shape Factor Correlations	18
2.7 Summary of the Equations and Method of Solution	21
3.0 RESULTS	22
4.0 CONCLUSIONS	37
REFERENCES	38

ILLUSTRATIONS

Figure

1. Correlation of the Shape Factor $H\delta^*$ for Adiabatic Flow	20
2. Correlation of the Shape Factor $H\theta^*$ for Adiabatic Flow	20
3. Correlation of the Shape Factor $H\delta^{**}$ for Adiabatic Flow	21
4. Correlation of the Compressible to Incompressible Momentum Thickness Ratio for Adiabatic Flow	21
5. Present Calculations and Incompressible Experimental Measurements of Schubauer and Klebanoff (IDENT = 2100, Ref. 18)	23
6. Favorable and Adverse Pressure Gradient Incompressible Velocity Profiles of Schubauer and Klebanoff (IDENT = 2100, Ref. 18)	24
7. Present Calculations and Incompressible Experimental Measurements of Stratford (IDENT = 5300, Ref. 18)	25
8. Severe Adverse Pressure Gradient Incompressible Velocity Profiles of Stratford (IDENT = 5300, Ref. 18)	26
9. Upper Surface Pressure Distributions on the RAE 2822 Airfoil for Cases 2, 9, and 12 of Ref. 19	26

<u>Figure</u>	<u>Page</u>
10. Upper Surface Boundary-Layer Properties of the RAE 2822 Airfoil for $M_{\infty} = 0.676$, $Re_{\infty,c} = 5.7 \times 10^6$, and $\alpha = -2.18$ deg (Case 2)	27
11. Upper Surface Boundary-Layer Properties of the RAE 2822 Airfoil for $M_{\infty} = 0.730$, $Re_{\infty,c} = 6.5 \times 10^6$, and $\alpha = 3.19$ deg (Case 9)	27
12. Upper Surface Boundary-Layer Properties of the RAE 2822. Airfoil for $M_{\infty} = 0.730$, $Re_{\infty,c} = 2.7 \times 10^6$, and $\alpha = 3.19$ deg (Case 12)	28
13. Velocity Profiles in the Shock Region of the RAE 2822 Airfoil for $M_{\infty} = 0.730$, $Re_{\infty,c} = 6.5 \times 10^6$, and $\alpha = 3.19$ deg (Case 9)	29
14. Velocity Profiles in the Shock Region of the RAE 2822 Airfoil for $M_{\infty} = 0.730$, $Re_{\infty,c} = 2.7 \times 10^6$, and $\alpha = 3.19$ deg (Case 12)	29
15. Boundary-Layer Displacement and Momentum Thickness Distributions for a Compressible Adiabatic Wall Boundary Layer with a Favorable Pressure Gradient	30
16. Pressure Distributions on the Waisted Body of Revolution for $M_{\infty} = 0.597$, $Re_{\infty,\ell} = 9.98 \times 10^6$ and $M_{\infty} = 1.398$, $Re_{\infty,\ell} = 10.08 \times 10^6$ (Ref. 21)	31
17. Boundary-Layer Properties on the Waisted Body of Revolution for $M_{\infty} = 0.597$ and $Re_{\infty,\ell} = 9.98 \times 10^6$	32
18. Boundary-Layer Properties on the Waisted Body of Revolution for $M_{\infty} = 1.398$ and $Re_{\infty,\ell} = 10.08 \times 10^6$	33
19. Velocity Profiles on the Waisted Body of Revolution for $M_{\infty} = 0.597$ and $Re_{\infty,\ell} = 9.98 \times 10^6$	34
20. Velocity Profiles on the Waisted Body of Revolution for $M_{\infty} = 1.398$ and $Re_{\infty,\ell} = 10.08 \times 10^6$	35
21. Influence of Initial Conditions on the Waisted Body of Revolution for $M_{\infty} = 0.597$ and $Re_{\infty,\ell} = 9.98 \times 10^6$	35
22. Calculated and Measured Skin Friction Distributions on the Waisted Body of Revolution for $M_{\infty} = 1.398$ and $Re_{\infty,\ell} =$ 10.08×10^6	36
23. Calculated and Measured Momentum Thickness Distributions on the Waisted Body of Revolution for $M_{\infty} = 1.398$ and $Re_{\infty,\ell} = 10.08 \times 10^6$	36

TABLE

1. Summary of Procedure for Computation of Turbulent Boundary-Layer Velocity Distributions 15

APPENDIX

A. LISTING OF THE BOUNDARY-LAYER COMPUTER CODE	41
NOMENCLATURE	45

1.0 INTRODUCTION

The present work is a result of efforts directed toward providing theoretical support to aerodynamic testing in transonic wind tunnels. The corresponding boundary-layer problems usually involve compressible turbulent flows with both favorable and adverse pressure gradients on smooth impermeable adiabatic walls. The following requirements have occurred in the Propulsion Wind Tunnel Facility (PWT) at the Arnold Engineering Development Center (AEDC) which illustrate the need to solve this sort of boundary-layer problem rapidly, with reasonable accuracy, and with minimal preparation time: (1) support of tests while they are in the tunnel, (2) accounting for the boundary-layer displacement effect in solutions requiring viscous/inviscid iterations, and (3) estimation of skin friction drag. In the first requirement, quick results are desired to investigate boundary-layer problems that could influence the remaining test plan. In the second requirement, transonic inviscid codes can be complicated and require large amounts of computer time and storage; hence it is desirable to expend minimum time, effort, and computer resources on the boundary-layer portion of the problem. For the last requirement, it is usually necessary to perform computations for a large number of test conditions and it is desirable to reduce the time per solution to conserve computer time. The present work was carried out to yield a turbulent boundary-layer calculation method capable of providing reasonably accurate solutions in short periods of time with minimal demands on computer resources.

Turbulent boundary-layer computation methods can be divided into two classes, integral and differential techniques. Integral methods require the solution to one, or more, ordinary differential equations, but differential methods require the solution to a system of partial differential equations. As a result, development of differential methods has accelerated in recent years following advances in computational capabilities (including both computers and numerical algorithms), whereas integral methods require less in the way of computational capability and have been under investigation for many years. Differential methods, in conjunction with improved turbulence models such as the one- or two-equation-of-turbulence models, are usually regarded as more accurate than integral methods for general applications (Ref. 1). With regard to specific applications, however, the results of the Stanford Conference (Ref. 2) on incompressible flow indicate that some integral techniques provide essentially the same accuracy as differential methods. Therefore, an integral approach is considered here in the interest of simplicity and speed, with the additional intent of developing an integral method to the point of being competitive in accuracy with differential methods for transonic turbulent flow over an adiabatic wall.

The approach of this work is the simultaneous solution of the momentum integral equation and the mean-flow kinetic energy integral equation for two-dimensional planar

or axisymmetric flow. The momentum integral equation is usually used in integral methods (an exception to this is White's (Ref. 3) method; he contends that his technique is entirely different from von Kármán's momentum integral equation). Use of the mean-flow kinetic energy integral equation is not uncommon in integral techniques, but it is not universal. A primary advantage of using this latter equation was pointed out by Nash (Ref. 4) to be that it is extendible to compressible flow without the transformation limitations associated with the moment-of-momentum integral equation.

In addition to the momentum integral equation and the mean-flow kinetic energy integral equation, other auxiliary parameters commonly required for solution of the integral equations are addressed:

1. The wall shear stress
2. Velocity profiles
3. The shear-work integral
4. The velocity-temperature relationship
5. Shape factor correlations

The methods by which items 2 through 4 are handled in the present work are different from those used in other integral techniques. The velocity profile is a newly developed profile which promises increased accuracy, the shear-work integral is evaluated directly rather than by empirical correlation, and the temperature (density) distribution is based on a new relation which predicts the total-temperature overshoot near the outer edge of turbulent adiabatic wall boundary layers with nonunity Prandtl number and recovery factor.

The integral method is developed in Section 2.0. Numerical solutions are compared with experiments and finite difference boundary-layer solutions in Section 3.0 to establish the capabilities and limitations of the method. These solutions are all for an adiabatic wall as this is the situation usually encountered in transonic flow applications. The resulting computer program used to obtain the results is short and simple to use. A listing of the Fortran code is presented in Appendix A.

2.0 ANALYSIS

The general form of the integral boundary-layer equations for x-momentum and mean-flow kinetic energy for turbulent compressible flow on two-dimensional planar or axisymmetric bodies is derived in this section. The five items, which amount to auxiliary relations, mentioned in the preceding section will be addressed as they arise in the development of the integral method. The numerical method used to solve the equations is a simple one used by Nash (Ref. 4).

2.1 DERIVATION OF THE INTEGRAL EQUATIONS

The compressible turbulent boundary-layer equations of continuity, x-momentum, and total enthalpy (energy) are, respectively,

$$\frac{\partial}{\partial x} \left(r^k \rho u \right) + \frac{\partial}{\partial y} \left(r^k \rho v \right) = 0 \quad (1)$$

$$\rho u \frac{\partial u}{\partial x} + \rho v \frac{\partial u}{\partial y} = - \frac{dp}{dx} + \frac{1}{r^k} \frac{\partial}{\partial y} \left[r^k \left(\mu \frac{\partial u}{\partial y} - \rho \overline{u'v'} \right) \right] \quad (2)$$

$$\rho u \frac{\partial H}{\partial x} + \rho v \frac{\partial H}{\partial y} = \frac{1}{r^k} \frac{\partial}{\partial y} \left\{ r^k \left[\left(\frac{\mu}{Pr} - \frac{\rho \epsilon}{Pr_t} \right) \frac{\partial H}{\partial y} + \mu \left(1 - \frac{1}{Pr} \right) u \frac{\partial u}{\partial y} - \rho \epsilon \left(1 - \frac{1}{Pr_t} \right) u \frac{\partial u}{\partial y} \right] \right\} \quad (3)$$

where $r = r_w + y \cos \psi$ for external flow, $r = r_w - y \cos \psi$ for internal flow, $k = 0$ for two-dimensional planar flow, and $k = 1$ for axisymmetric flow. The dependent variables in Eqs. (1) through 3 are time-averaged quantities with the exception of the term ρv , which is actually the product of the time-averaged ρ and the mass-weighted averaged v (see Cebeci and Smith (Ref. 5) for a discussion of the approximations leading to the boundary-layer equations). The y -momentum equation is $\partial p / \partial y = 0$. The momentum and mean-flow kinetic energy integral equations will be derived from Eqs. (1) and (2). Equation (3) is the basis for a relation between velocity and temperature which is required for solution of the compressible momentum and mean-flow kinetic energy integral equations.

The momentum and mean-flow kinetic energy integral equations are derived by multiplying Eq. (1) by $u^{m+1}/(m+1)$, Eq. (2) by $r^k u^m$ summing, and simplifying the results to obtain

$$\frac{1}{m+1} \left[\frac{\partial (r^k \rho u^{m+2})}{\partial x} + \frac{\partial (r^k \rho v u^{m+1})}{\partial y} \right] = -r^k u^m \frac{dp}{dx} + u^m \frac{\partial (r^k r)}{\partial y} \quad (4)$$

where τ is the total shear stress

$$\tau = \mu \frac{\partial u}{\partial y} - \rho \overline{u'v'} \quad (5)$$

Substitution of $m = 0$ will eventually result in the momentum integral equation, and $m = 1$ in the mean-flow kinetic energy integral equation. Using the momentum equation at the edge of the boundary layer

$$\frac{dp}{dx} = -\rho_e u_e \frac{du_e}{dx} \quad (6)$$

and subtracting the term $1/(m+1) \partial/\partial x r^k \rho u u_e^{m+1}$ from each side of Eq. (4), one can write the expression

$$\begin{aligned} \frac{1}{m+1} \left\{ \frac{\partial}{\partial x} \left[r^k \rho_e u_e^{m+2} \frac{\rho u}{\rho_e u_e} \left(\frac{u^{m+1}}{u_e^{m+1}} - 1 \right) \right] + \frac{\partial}{\partial y} \left(r^k \rho v u^{m+1} \right) \right\} \\ = r^k u^m u_e \rho_e \frac{du_e}{dx} - \frac{1}{m+1} \frac{\partial}{\partial x} \left(r^k \rho u u_e^{m+1} \right) + u^m \frac{\partial}{\partial y} (r^k r) \end{aligned} \quad (7)$$

Expanding the middle term on the right-hand side of Eq. (7), combining part of this expansion with the term containing du_e/dx , and using Eq. (1) in the remaining portion of the expansion results in the expression

$$\begin{aligned} \frac{1}{m+1} \left\{ \frac{\partial}{\partial x} \left[r^k \rho_e u_e^{m+2} \frac{\rho u}{\rho_e u_e} \left(\frac{u^{m+1}}{u_e^{m+1}} - 1 \right) \right] + \frac{\partial}{\partial y} \left(r^k \rho v u^{m+1} \right) - u_e^{m+1} \frac{\partial}{\partial y} (r^k \rho v) \right\} \\ = r^k \rho_e u_e^{m+1} \frac{du_e}{dx} \left(\frac{u^m}{u_e^m} - \frac{\rho u}{\rho_e u_e} \right) + u^m \frac{\partial}{\partial y} (r^k r) \end{aligned} \quad (8)$$

Integrating Eq. (8) with respect to y over the interval $(0 \leq y < \infty)$ yields the result

$$\begin{aligned} \frac{1}{m+1} \left\{ \int_0^\infty \frac{\partial}{\partial x} \left[r^k \rho_e u_e^{m+2} \frac{\rho u}{\rho_e u_e} \left(\frac{u^{m+1}}{u_e^{m+1}} - 1 \right) \right] dy + u_e^{m+1} r_w^k \rho_w v_w \right\} \\ = \int_0^\infty r^k \rho_e u_e^{m+1} \frac{du_e}{dx} \left(\frac{u^m}{u_e^m} - \frac{\rho u}{\rho_e u_e} \right) dy + \int_0^\infty u^m \frac{\partial}{\partial y} (r^k r) dy \end{aligned} \quad (9)$$

The no-slip wall boundary condition of $u = 0$ at $y = 0$ is used to obtain Eq. (9). In addition, two terms resulting from the integration of the second and third terms on the left-hand side of Eq. (8) do not appear in Eq. (9) because they sum to zero as a consequence of $\rho v \rightarrow (\rho v)_e$ and $u \rightarrow u_e$ in the limit of $y \rightarrow \infty$.

For the special case of $m = 0$, Eq. (9) can be written

$$\begin{aligned} \int_0^\infty \frac{\partial}{\partial x} \left[r^k \rho_e u_e^2 \frac{\rho u}{\rho_e u_e} \left(1 - \frac{u}{u_e} \right) \right] dy + \int_0^\infty r^k \rho_e u_e \frac{du_e}{dx} \left(1 - \frac{\rho u}{\rho_e u_e} \right) dy \\ - r_w^k u_e \rho_w v_w = r_w^k \tau_w \end{aligned} \quad (10)$$

In writing Eq. (10), it is necessary to use $(r^k \tau) \rightarrow 0$ as $y \rightarrow \infty$. To show that $(r^k \tau) \rightarrow 0$ as $y \rightarrow \infty$, consider the following: The turbulence model used subsequently in this analysis will postulate the shear stress in the outer part of the boundary layer to be proportional to the local velocity gradient. Therefore, because r is linear in y , it will suffice to prove that $(y \partial u / \partial y) \rightarrow 0$ as $y \rightarrow \infty$. As a consequence of the velocity profile developed in Ref. 6, also to be used subsequently in this analysis, the term $\partial u / \partial y$ behaves as $\exp(-cy^b)$ where $c > 0$ and $b > 0$. The product $y \exp(-cy^b) \rightarrow 0$ as $y \rightarrow \infty$, and hence $(r^k \tau) \rightarrow 0$ as $y \rightarrow \infty$.

For the special case of $m = 1$, Eq. (9) can be written

$$\frac{1}{2} \int_0^\infty \frac{\partial}{\partial x} \left[r^k \rho_e u_e^3 \frac{\rho u}{\rho_e u_e} \left(1 - \frac{u^2}{u_e^2} \right) dy \right] + \int_0^\infty r^k \rho_e u_e^2 \frac{du_e}{dx} \frac{u}{u_e} \left(1 - \frac{\rho}{\rho_e} \right) dy - \frac{1}{2} r_w^k u_e^2 \rho_w v_w = \int_0^\infty r^k \tau \frac{\partial u}{\partial y} dy \quad (11)$$

In writing Eq. (11), it is necessary to integrate the last term in Eq. (9) by parts and again use $(r^k \tau) \rightarrow 0$ as $y \rightarrow \infty$.

Interchanging the order of differentiation and integration in Eqs. (10) and (11), these equations can be written as

$$\frac{1}{r_w^k \rho_e u_e^2} \frac{d}{dx} \left(r_w^k \rho_e u_e^2 \tilde{\theta} \right) + \frac{\tilde{\delta}^*}{u_e} \frac{du_e}{dx} - \frac{\rho_w v_w}{\rho_e u_e} = \frac{c_f}{2} \quad (12)$$

$$\frac{1}{2 r_w^k \rho_e u_e^3} \frac{d}{dx} \left(r_w^k \rho_e u_e^3 \tilde{\theta}^* \right) + \frac{\tilde{\delta}^{**}}{u_e} \frac{du_e}{dx} - \frac{1}{2} \frac{\rho_w v_w}{\rho_e u_e} = \frac{c_f}{2} \tilde{D} \quad (13)$$

where

$$\frac{c_f}{2} = \frac{r_w}{\rho_e u_e^2} \quad (14)$$

$$\tilde{\theta} = \int_0^\infty \frac{\rho u}{\rho_e u_e} \left(1 - \frac{u}{u_e} \right) \left(1 \pm \frac{y}{r_w} \cos \psi \right)^k dy \quad (15)$$

$$\tilde{\theta}^* = \int_0^\infty \left(1 - \frac{\rho u}{\rho_e u_e} \right) \left(1 \pm \frac{y}{r_w} \cos \psi \right)^k dy \quad (16)$$

$$\tilde{\theta}^{**} = \int_0^\infty \frac{\rho u}{\rho_e u_e} \left(1 - \frac{u^2}{u_e^2} \right) \left(1 \pm \frac{y}{r_w} \cos \psi \right)^k dy \quad (17)$$



$$\tilde{\delta}^{**} = \int_0^\infty \frac{u}{u_e} \left(1 - \frac{\rho}{\rho_e} \right) \left(1 \pm \frac{y}{r_w} \cos \psi \right)^k dy \quad (18)$$

$$\tilde{D} = \int_0^\infty \frac{r}{r_w} \frac{\partial(u/u_e)}{\partial y} \left(1 \pm \frac{y}{r_w} \cos \psi \right)^k dy \quad (19)$$

These five integral quantities are denoted by the tilde (~) in order to distinguish them from true defect lengths. For example, $\tilde{\delta}^*$ defined by Eq. (16) is the true mass-flow defect (displacement) length for two-dimensional planar flow ($k = 0$) but it is not the true mass-flow defect length for axisymmetric flow ($k = 1$) (see Ref. 7). However, $\tilde{\delta}^*$ approaches the true mass-flow defect length for axisymmetric flow when the boundary layer is thin compared to the local body radius. This is true not only because y/r_w in Eq. (16) is small when $(1-\rho u/\rho_e u_e)$ is largest, but also because δ^*/r_w (a term not appearing in Eq. (16) but that does appear in the true expression for the mass-flow defect length, see, e.g., Section 1.9 of Ref. 5) is small compared to unity. It is important to make this point about the defect lengths because if Eq. (16) was used to compute the displacement effect on an axisymmetric body with thick boundary layers for use in a viscous/inviscid iteration calculation, for example, the computed displacement effect would be incorrect. Although the lengths defined by Eqs. (15) through (18) are not true defect lengths for axisymmetric flow, Eqs. (12) and (13) are exact within the boundary-layer approximation and are the general form of the momentum and mean-flow kinetic energy integral equations for compressible flow on two-dimensional planar or axisymmetric bodies.

The analysis is hereafter restricted to boundary layers that are thin relative to the local body radius. The motivation for this is that by excluding the term $(y/r_w) \cos \psi$ in Eqs. (15) through (18), integrations can be performed once and for all in order to establish correlations for certain shape factors which will appear in the analysis. Otherwise, integration of Eqs. (15) through (18) has to be performed at each axial station thereby increasing the computational time. The analysis is also restricted at this point to an impermeable wall, $v_w = 0$. It would be a trivial program modification to include the permeable wall capability, but the associated auxiliary relations were not investigated as to their suitability for use in permeable wall calculations. For thin boundary layers relative to the local body radius, and for impermeable walls, the momentum and mean-flow kinetic energy integral equations, [Eqs. (12) and (13)], reduce to

$$\frac{1}{r_w^k \rho_e u_e^2} \frac{d}{dx} \left(r_w^k \rho_e u_e^2 \theta \right) - \frac{\delta^*}{u_e} \frac{du_e}{dx} = \frac{c_f}{2} \quad (20)$$

$$\frac{1}{2 r_w^k \rho_e u_e^3} \frac{d}{dx} \left(r_w^k \rho_e u_e^3 \theta^* \right) + \frac{\delta^{**}}{u_e} \frac{du_e}{dx} = \frac{c_f}{2} D \quad (21)$$

where

$$\theta = \int_0^\infty \frac{\rho u}{\rho_e u_e} \left(1 - \frac{u}{u_e} \right) dy \quad (22)$$

$$\delta^* = \int_0^\infty \left(1 - \frac{\rho u}{\rho_e u_e} \right) dy \quad (23)$$

$$\theta^* = \int_0^\infty \frac{\rho u}{\rho_e u_e} \left(1 - \frac{u^2}{u_e^2} \right) dy \quad (24)$$

$$\delta^{**} = \int_0^\infty \frac{u}{u_e} \left(1 - \frac{\rho}{\rho_e} \right) dy \quad (25)$$

$$D = \int_0^\infty \frac{\tau}{\tau_w} \frac{\partial(u/u_e)}{\partial y} dy \quad (26)$$

Equations (20) through (26) are used in this work, where $k = 0$ for planar flow and $k = 1$ for axisymmetric flow. (Actually, in the computer program, planar flow is handled by inputting $r_w = \text{constant}$.)

2.2 WALL SHEAR STRESS

An expression is needed for the local skin friction coefficient appearing in Eqs. (20) and (21) in terms of variables appearing in these equations. Such expressions are frequently derived by using the zero pressure gradient ($dp/dx = 0$) momentum equation to develop a transformation relating the compressible skin friction coefficient, c_f , to an incompressible skin friction coefficient, \bar{c}_f . One of the available expressions for \bar{c}_f can then be used to determine c_f . In the present work, variable pressure gradient ($dp/dx \neq 0$) as well as zero pressure gradient flows are of interest and the procedure for obtaining an expression for c_f is not well established. Therefore, the rationale behind the one developed here will be given; the success of the resulting expression will be judged by the agreement obtained with experimental data.

The basis for the present expression for c_f is Coles' law of corresponding stations (Ref. 8) which is

$$c_f \overline{Re}_\theta = \frac{\rho_e \mu_e}{\rho_w \mu_w} \bar{c}_f \overline{Re}_\theta \quad (27)$$

where the superscript bar ($\bar{\cdot}$) denotes low-speed flow. This relation was used by Lewis, Kubota, and Webb (Ref. 9), along with the approximation, $\mu \sim T$, to successfully

correlate high-speed (up to $M_e = 8.18$) turbulent boundary-layer velocity profiles. Using this approximation, i.e., $\mu \sim T$, Eq. (27) reduces to

$$c_f \text{Re}_\theta = \bar{c}_f \bar{\text{Re}}_\theta \quad (28)$$

It was pointed out in Refs. 8 and 9 that, whereas Eq. (27) specifies the relation for corresponding stations, it does not specify the relation between c_f and \bar{c}_f , which must come from hypothesis. In this work, recourse is made to the work of Winter and Gaudet (Ref. 10), who established the relation

$$\frac{\bar{c}_f}{c_f} = F_c = \left(1 + \frac{M_e^2}{5}\right)^{1/2} \quad (29)$$

for adiabatic walls, $dp/dx = 0$, and air. It is hypothesized that Eq. (29) is acceptable for $dp/dx \neq 0$ if an appropriate expression is used for \bar{c}_f for $dp/dx \neq 0$. The expression used for \bar{c}_f is

$$\bar{c}_f = \frac{0.3e^{-1.33\bar{H}}}{(\log_{10} \bar{\text{Re}}_\theta)^{1.74+0.31\bar{H}}} \quad (30)$$

which is Eq. (6-179) in White's book (Ref. 3). The incompressible momentum thickness Reynolds number, $\bar{\text{Re}}_\theta$, used in Eq. (30) is obtained using Eqs. (28), (29), and Re_θ , which is calculated as part of the solution. The incompressible shape factor, \bar{H} , used in Eq. (30) is obtained by a subsequently developed correlation of \bar{H} as a function of H_δ^* (which is also calculated as part of the solution) and M_e .

2.3 VELOCITY PROFILE

The integrals of Eqs. (22) to (25) are usually evaluated by use of power-law or law-of-the-wake (Ref. 11) velocity profiles. The main feature distinguishing the current method from previous integral methods and the main contribution to the quality of the results is the use of a newly developed velocity profile. This new profile is given by a closed-form analytical expression valid over the entire thickness of the turbulent boundary layer, Ref. 6. Shown in step 8 of Table 1, the expression is the sum of two transcendental functions, one expressed in terms of the inner variable, y^+ , and one expressed in terms of the outer variable, $y/\bar{\theta}$. Table 1 was taken from Ref. 6 and is a summary of the procedure for calculating turbulent boundary-layer velocity profiles by this method. This expression was shown in Ref. 6 to provide a reasonably accurate means of correlating various velocity profiles that included boundary layers near separation, reattached boundary layers, nonequilibrium boundary layers (boundary layers with nonzero streamwise variation of β), and compressible boundary layers. In the latter case, the incompressible profile given in Table 1 is related to the corresponding compressible

profile by $u/u_e = \bar{u}/\bar{u}_e$ and $y/\bar{\theta} = (y/\theta)(\theta/\bar{\theta})$ where $\theta/\bar{\theta}$ is a correlation developed in Subsection 2.6. It is convenient that the expression for the profile is a function of the local incompressible parameters: skin friction coefficient, shape factor, and Reynolds number based on momentum thickness, because these parameters are a natural consequence of the equations being solved. This velocity profile expression was developed

Table 1. Summary of Procedure for Computation of Turbulent Boundary-Layer Velocity Distributions

Step	Requirement	Comment
1.	$H, \bar{u}_e^+,$ and \bar{Re}_0 are inputs (use incompressible values)	$\bar{u}_e^+ = \left(\frac{2}{c_f}\right)^{1/2}$
2.	Compute $\frac{\bar{u}}{\bar{u}_e} (2) = 1.723 e^{-0.6 H} \left(1 + \frac{50}{\bar{Re}_0}\right)$	$\frac{\bar{u}}{\bar{u}_e} \left(\frac{y}{\theta}\right)$ at $\frac{y}{\theta} = 2$
3.	Compute $\frac{\bar{u}}{\bar{u}_e} (5) = 0.87 + 0.08e^{-2.6(H-1.95)^2}$	$\frac{\bar{u}}{\bar{u}_e} \left(\frac{y}{\theta}\right)$ at $\frac{y}{\theta} = 5$
4.	Compute $g(2) = \frac{\frac{\bar{u}}{\bar{u}_e} (2) - \frac{1}{0.09 \bar{u}_e^+} \tan^{-1} \left(\frac{0.18 \bar{Re}_0}{\bar{u}_e^+}\right)}{1 - \frac{\pi}{0.18 \bar{u}_e^+}}$	$g\left(\frac{y}{\theta}\right)$ at $\frac{y}{\theta} = 2$
5.	Compute $g(5) = \frac{\frac{\bar{u}}{\bar{u}_e} (5) - \frac{1}{0.09 \bar{u}_e^+} \tan^{-1} \left(\frac{0.45 \bar{Re}_0}{\bar{u}_e^+}\right)}{1 - \frac{\pi}{0.18 \bar{u}_e^+}}$	$g\left(\frac{y}{\theta}\right)$ at $\frac{y}{\theta} = 5$
6.	Compute $b = \frac{\ln \left(\frac{\tanh^{-1} [g^2(2)]}{\tanh^{-1} [g^2(5)]} \right)}{\ln \left(\frac{2}{5} \right)}$	$\tanh^{-1} z = \frac{1}{2} \ln \left(\frac{1+z}{1-z} \right)$
7.	Compute $a = \frac{\tanh^{-1} [g^2(2)]}{2b}$	$\tanh z = \frac{e^{2z} - 1}{e^{2z} + 1}$
8.	$(\bar{u}^+) = \frac{1}{0.09} \tan^{-1} (0.09 y^+) + \left(\bar{u}_e^+ - \frac{\pi}{0.18}\right) \tanh^{1/2} \left[a \left(\frac{y}{\theta} \right)^b \right]$	$\frac{\bar{u}}{\bar{u}_e} = \frac{\bar{u}}{\bar{u}_e^+}$ $\frac{\bar{u}}{\bar{u}_e} = \frac{\bar{u}^+}{\bar{u}_e^+}$ $y^+ = \frac{\bar{Re}_0}{\bar{u}_e^+} \cdot \frac{y}{\theta}$

for two-dimensional planar flows, but it is used herein for axisymmetric flows without modification, because the assumption has been made that the boundary layer is thin relative to the local body radius.

Because the new profile reduces to an identity at the wall, it is not possible to calculate the wall shear stress, $\tau_w = (\mu \partial u / \partial y)_w$, by taking the slope of the velocity profile. Instead, the wall shear is obtained from the skin friction coefficient developed in Subsection 2.2. The shear work integral, Eq. (26), is usually obtained by correlation of experimental data, but the new velocity profile is considered sufficiently accurate to permit evaluation of Eq. (26) by use of $\partial u / \partial y$ obtained from the profile expression and an appropriate turbulence model, as described in Subsection 2.4.

2.4 SHEAR-WORK INTEGRAL

The term referred to here as the shear-work integral (also frequently referred to in the literature as the dissipation integral) is denoted by D and given by Eq. (26). The velocity profile given in Table 1 is used to compute the velocity derivative, and in this regard it is convenient to express Eq. (26) as

$$D = \int_0^\infty \frac{\tau}{\tau_w} \frac{\partial(u - u_e)}{\partial(y/\bar{\theta})} dy \quad (31)$$

inasmuch as $y/\bar{\theta}$ is one of the independent variables in the velocity expression. The problem, therefore, is to specify the shear-stress distribution, τ/τ_w , across the boundary layer in order to carry out the integration identified by Eq. (31). In keeping with the idea of maintaining simplicity, the shear-stress distribution is specified in three regions across the boundary layer, and common turbulence models for each region are used.

The first region considered is that near the wall, defined by $0 \leq y^+ \leq 100$. In deriving the inner solution part of the velocity profile in Table 1 (the inner solution part is $\tan^{-1}(0.09 y^+)/0.09$), it was assumed that the total shear stress τ was constant and equal to τ_w . Based on the agreement between experimental data and the velocity profile expression resulting from this assumption (see Ref. 6), it appears that $\tau = \tau_w$ for $0 \leq y^+ \leq 100$ is a plausible approximation for use in Eq. (31). In fact, in Fig. 7 of Ref. 6 an extreme case of an experimental velocity profile having a severe adverse pressure gradient and no logarithmic region was well represented by the velocity expression in Table 1, and for this case the inner solution, $\tan^{-1}(0.09 y^+)/0.09$, was the dominant term for $0 \leq y^+ \leq 100$. The assumption $\tau = \tau_w$ allows Eq. (31) to be integrated analytically over $0 \leq y^+ \leq 100$ (i.e., out to the value of $y/\bar{\theta}$ where $y^+ = 100$ as given by $y/\bar{\theta} = 100 \bar{u}_e^+ / \bar{Re}_\theta$, see Table 1) and numerical integration is avoided.

The next two regions are handled by Boussinesq's (Ref. 12) eddy-viscosity concept, where the eddy viscosity ϵ is defined by

$$\overline{-u'v'} = \epsilon \frac{\partial u}{\partial y} \quad (32)$$

where ϵ will be either ϵ_m or ϵ_o , depending on the region. For the first region outside $y^+ = 100$ (middle region), Prandtl's mixing-length theory (Ref. 12) is used where

$$\epsilon_m = \rho^2 \left| \frac{\partial u}{\partial y} \right| \quad (33)$$

and the mixing length is

$$\ell = 0.41y \quad (34)$$

For the outer region a constant eddy viscosity of the form suggested by Clauser (Ref. 13) is used. The specific expression for ϵ_o in the outer region is

$$\epsilon_o = 0.0168 u_e \bar{\delta}^* \quad (35)$$

where $\bar{\delta}^*$ is the incompressible displacement thickness defined as

$$\bar{\delta}^* = \int_0^\infty \left(1 - \frac{u}{u_e} \right) dy \quad (36)$$

The point in the boundary layer separating the middle region from the outer region at a particular x location is that point where $\epsilon_m = \epsilon_o$. The shear stress for $y^+ > 100$ primarily consists of the turbulent shear stress as defined by

$$\tau_t = -\rho \overline{u'v'} \quad (37)$$

and the shear stress distribution for use in Eq. (31) is approximated as

$$\frac{\tau}{\tau_w} = \frac{\rho (0.41y)^2 \left| \frac{\partial u}{\partial y} \right| \frac{\partial u}{\partial y}}{\tau_w} = \frac{2}{c_f} \frac{\rho}{\rho_e} \left(0.41 \frac{y}{\bar{\delta}} \right)^2 \left| \frac{\partial \left(\frac{u}{u_e} \right)}{\partial \left(\frac{y}{\bar{\delta}} \right)} \right| \frac{\partial \left(\frac{u}{u_e} \right)}{\partial \left(\frac{y}{\bar{\delta}} \right)} \quad (38)$$

for the middle region, and

$$\frac{\tau}{\tau_w} = \frac{0.0168 \rho u_e \bar{\delta}^* \frac{\partial u}{\partial y}}{\tau_w} = 0.0168 \frac{2}{c_f} \frac{\rho}{\rho_e} \bar{H} \frac{\partial \left(\frac{u}{u_e} \right)}{\partial \left(\frac{y}{\bar{\delta}} \right)} \quad (39)$$

for the outer region.

Equation (31) is analytically integrated from $y^+ = 0$ to $y^+ = 100$ and then numerically integrated in the middle and outer regions, using Eqs. (38) and (39) with ρ/ρ_e being evaluated as discussed in Subsection 2.5.

2.5 VELOCITY-TEMPERATURE RELATIONS

To establish the necessary shape factor correlations for use in the solution to Eqs. (20) and (21) it is necessary to use a relation between velocity and temperature in order

to integrate Eqs. (22) to (25) (recall that $\rho/\rho_e = T_e/T$ as a consequence of $\partial p/\partial y = 0$). The relationship used is the analytical solution developed in Ref. 14 for nonunity Prandtl number. Because the interest here is in turbulent boundary layers on adiabatic walls, only the adiabatic wall solution in Ref. 14 is used. The advantage of the method developed in Ref. 14 over the more commonly used method of Crocco (Ref. 15) is that the results obtained in Ref. 14 predict the overshoot in total temperature near the outer edge of a turbulent boundary layer on an adiabatic wall [see, e.g., van Driest (Ref. 16)], which the Crocco results cannot do. Moreover, the Crocco solution is actually contained as a special case of the solution given in Ref. 14 for unity Prandtl numbers. The quality of agreement between the results of Ref. 14 and experimental data is considered good. The comparisons from which this conclusion was drawn are given in Refs. 14 and 17.

The density ratio in the expressions for the shear-stress distributions, Eqs. (38) and (39), is, however, specified by the modified Crocco relation for an adiabatic wall (see, e.g., Ref. 3)

$$\rho_e/\rho = T/T_e = 1 + r(\gamma - 1) M_e^2 (1 - u^2/u_e^2)/2$$

The reason for this choice rather than using Ref. 14 is that numerical integration of Eq. (31) is carried out at each axial location (whereas integrations for the shape factor correlations are carried out only one time) and the modified Crocco relation is simpler than the solution given in Ref. 14, requiring less computer time. Moreover, the modified Crocco relation is in good agreement with the solution given in Ref. 14 in the region near the wall for adiabatic flow and this region is the dominant portion of the integrand of Eq. (31).

2.6 SHAPE FACTOR CORRELATIONS

There are four length scales in Eqs. (20) and (21), θ , δ^* , θ^* , and δ^{**} . It is convenient and computationally expedient to correlate these lengths by analytical expressions of other variables to avoid evaluation of the integrations identified by Eqs. (22) through (25) at each x location (and possibly several times at each x location to obtain convergence). The approach is to define the following shape factors

$$H_{\delta^*} = \frac{\delta^*}{\theta} \quad (40)$$

$$H_{\theta^*} = \frac{\theta^*}{\theta} \quad (41)$$

and

$$H_{\delta^{**}} = \frac{\delta^{**}}{\theta} \quad (42)$$

$$\frac{T}{T_e} \approx 1 + \frac{r(\theta-1)}{2} M_e^2 \quad \frac{T}{T_0} = 1 + \frac{\theta-1}{2} M_e^2$$

AEDC-TR-78-42

and then correlate these shape factors in terms of M_e and \bar{H} where

$$\bar{H} = \frac{\delta^*}{\theta} \quad (43)$$

In addition, because y is scaled by $\bar{\theta}$ as shown in Table 1, and because θ is obtained from the solution to Eqs. (20) and (21), a correlation for $\theta/\bar{\theta}$ is also established.

The velocity profile given in Table 1 was used to carry out the numerical integrations (using Simpson's rule) necessary to establish the correlations. This profile depends on \bar{c}_f and \bar{Re}_θ as well as \bar{H} . Using Eq. (30) for $\bar{c}_f = \bar{c}_f(\bar{Re}_\theta, \bar{H})$, the variables are reduced to \bar{Re}_θ and \bar{H} only. The influence of \bar{Re}_θ on the numerical results is extremely small compared to that of \bar{H} . For example, the difference between solutions with $\bar{Re}_\theta = 5,000$ and $\bar{Re}_\theta = 100,000$ is less than one percent, which is within the accuracy of the analytical expressions derived for the correlations. All numerical results given here for the correlations are for $\bar{Re}_\theta = 50,000$.

The numerical results for H_{δ^*} , H_{θ^*} , $H_{\delta^{**}}$, and $\theta/\bar{\theta}$ are represented in Figs. 1 through 4 as open symbols. The results of the analytical expressions derived to represent these numerical results are given in Figs. 1 through 4 as solid lines. The analytical expressions derived by inspection are

$$H_{\delta^*} = \bar{H} \left(1 + 0.113 M_e^2 \right) + 0.290 M_e^2 \quad (44)$$

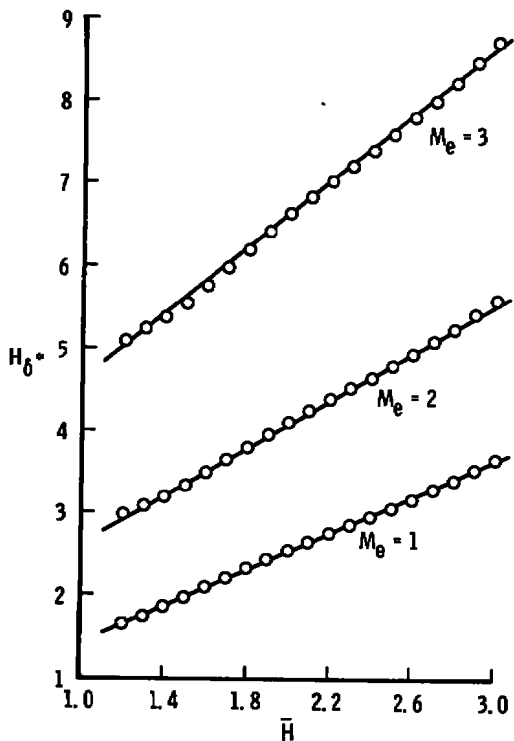
$$H_{\theta^*} = \frac{2 - 0.54 \tanh \left[1.1 (\bar{H} - 1) \right] + 0.028 M_e^2}{1 + 0.014 M_e^2} \quad (45)$$

$$H_{\delta^{**}} = \left(\frac{0.064}{\bar{H} - 0.8} + 0.251 \right) M_e^2 \quad (46)$$

and

$$\frac{\theta}{\bar{\theta}} = 1 - \frac{0.92 M_e^2}{7.09 + M_e^2} \tanh \left[1.49 (\bar{H} - 0.9) \right] \quad (47)$$

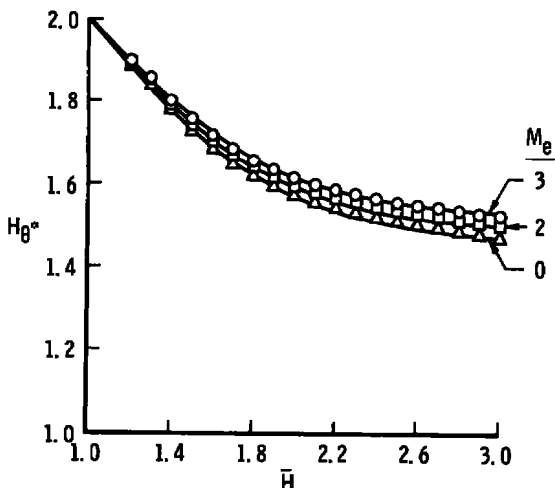
Although the constants differ, the general form of Eqs. (44) and (46) was used by Nash (Ref. 4) for these shape factor correlations. The form of Eq. (45) was not used by Nash, however. The advantage of Eq. (45) over the form used by Nash is that Eq. (45) can be inverted to obtain \bar{H} as a function of H_{θ^*} and M_e , which is useful in the numerical solution of Eqs. (20) and (21). The correlation given by Eq. (47) is in good agreement with that established by Winter and Gaudet (Ref. 10), although their correlation was for



Open Symbols Represent the Numerical Results for Eq. (40) Using the Velocity Profile Given in Table 1 and the Velocity-Temperature Relation of Ref. 14

Solid Curves Represent the Analytical Correlation of $H_{\delta^*} = \bar{H} (1 + 0.113 M_e^2) + 0.290 M_e^2$ [Eq. (44)]

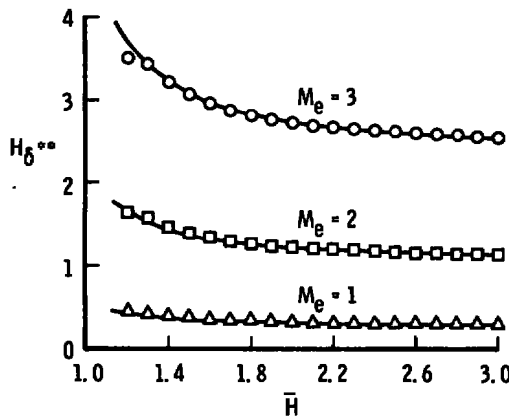
Figure 1. Correlation of the shape factor H_{δ^*} for adiabatic flow.



Open Symbols Represent the Numerical Results for Eq. (41) Using the Velocity Profile Given in Table 1 and the Velocity-Temperature Relation of Ref. 14

Solid Curves Represent the Analytical Correlation of $H_{\theta^*} = \frac{2 - 0.54 \tanh [1.1 (\bar{H} - 1)] + 0.028 M_e^2}{1 + 0.014 M_e^2}$ [Eq. (45)]

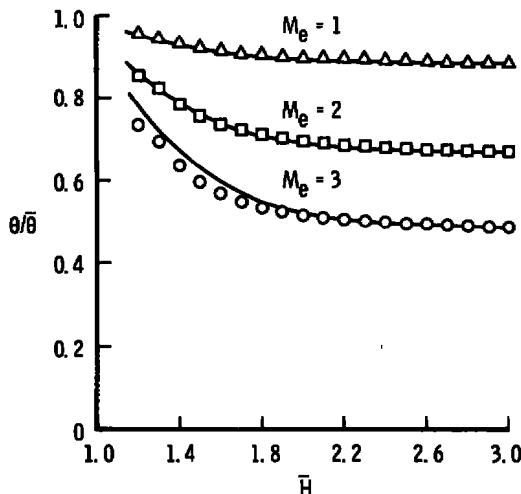
Figure 2. Correlation of the shape factor H_{θ^*} for adiabatic flow.



Open Symbols Represent the Numerical Results for Eq. (42) Using the Velocity Profile Given in Table 1 and the Velocity-Temperature Relation of Ref. 14
 Solid Curves Represent the Analytical Correlation of

$$H_{\delta}^{**} = \left(\frac{0.064}{\bar{H} - 0.8} + 0.251 \right) M_e^2 \quad [\text{Eq. (46)}]$$

Figure 3. Correlation of the shape factor H_{δ}^{**} for adiabatic flow.



Open Symbols Represent the Numerical Results for $\theta/\bar{\theta}$ Using the Velocity Profile Given in Table 1 and the Velocity-Temperature Relation of Ref. 14
 Solid Curves Represent the Analytical Correlation of

$$\frac{\theta}{\bar{\theta}} = 1 - \frac{0.92 M_e^2}{7.09 + M_e^2} \tanh [1.49 (\bar{H} - 0.9)] \quad [\text{Eq. (47)}]$$

Figure 4. Correlation of the compressible to incompressible momentum thickness ratio for adiabatic flow.

zero pressure gradient flows and did not contain the parameter \bar{H} . The correlations given by Eqs. (44) through (47) and compared with numerical results in Figs. 1 through 4 are for $M_e \leq 3$ and a constant recovery factor of 0.88.

2.7 SUMMARY OF THE EQUATIONS AND METHOD OF SOLUTION

Using the definitions of the shape factors defined by Eqs. (40) through (42), Eqs. (20) and (21) can be rewritten as

$$\frac{1}{r_w^k \rho_e u_e^2} \frac{d}{dx} \left(r_w^k \rho_e u_e^2 \theta \right) + H_{\delta^*} \frac{\theta}{u_e} \frac{du_e}{dx} = \frac{c_f}{2} \quad (48)$$

$$\frac{1}{2 r_w^k \rho_e u_e^3} \frac{d}{dx} \left(r_w^k \rho_e u_e^3 \theta H_{\theta^*} \right) + H_{\delta^{**}} \frac{\theta}{u_e} \frac{du_e}{dx} = \frac{c_f}{2} D \quad (49)$$

where H_{δ^*} , H_{θ^*} , and $H_{\delta^{**}}$ are given by Eqs. (44) through (46) and are functions of \bar{H} and M_e as indicated. The skin friction coefficient, c_f , used in the solution of Eqs. (48) and (49) is given by Eqs. (28) through (30) and can be written as

$$c_f = \frac{1}{F_c} \frac{0.3 e^{-1.33 \bar{H}}}{[\log_{10} (Re_\theta / F_c)]^{1.74 - 0.31 \bar{H}}} \quad (50)$$

where $F_c = (1 + M_e^2/5)^{1/2}$. The skin friction coefficient is, therefore, a function of \bar{H} , M_e , and Re_θ where $Re_\theta = \rho_e u_e \theta / \mu_e$. The shear-work integral, D , is defined by Eq. (31) where τ/τ_w is unity for $0 \leq y^+ \leq 100$, and given by Eqs. (38) and (39) for the middle and outer regions of the boundary layer. Therefore, D depends on c_f , \bar{H} , $\bar{\theta}$, and ρ/ρ_e (where ρ_e/ρ is given by the modified Crocco relation, Subsection 2.5). All of these quantities can be related to \bar{H} , M_e , and Re_θ (or θ in place of Re_θ because $\rho_e u_e / \mu_e$ is known from the boundary-layer edge conditions). Equations (48) and (49) are, therefore, two equations for the two unknowns \bar{H} and θ .

The method used to solve Eqs. (48) and (49) is the predictor-corrector method used by Nash (Ref. 4). Various schemes were tried for determining step size and for most problems the step size was not particularly important. A constant value for the step size was used for the solutions presented in this report; however, because the code is simple, it is a trivial task for the user to modify this portion of the program as appropriate. Initial values of θ and H (from which \bar{H} is obtained in the program using Eq. (44)) must be input as well as a reference Mach number, Reynolds number, and M_e and r_w as functions of x . A listing of the boundary-layer code is given in Appendix A.

3.0 RESULTS

Because a turbulent boundary-layer calculation method can be made to fit a particular set of experimental data, it is of interest to consider several sets of data for various conditions. The present method was applied to a large number of experiments and examples are presented in this section. The examples presented are those of Schubauer and Klebanoff (Ref. 18), Stratford (Ref. 18), Cook, McDonald, and Firmin

(Ref. 19), Pasiuk, Hastings, and Chatham (Ref. 20), and Winter, Rotta, and Smith (Ref. 21). These examples represent a fairly broad range of flow conditions that include favorable, mild, and severe adverse pressure gradients.

The experiment of Schubauer and Klebanoff (Ref. 18) was selected because it is a realistic airfoil-type flow commonly encountered and also numerous other calculation techniques were compared to this experiment in Ref. 2, from which indirect comparisons with the present method can be inferred. Comparisons between calculated and measured values of c_f , H_{δ^*} , and Re_{θ} are given in Fig. 5. The agreement is reasonably good upstream of about $x = 22.5$ ft. This is the same sort of agreement obtained by nearly all the 27 calculation techniques (both integral and finite difference) shown in Ref. 2.

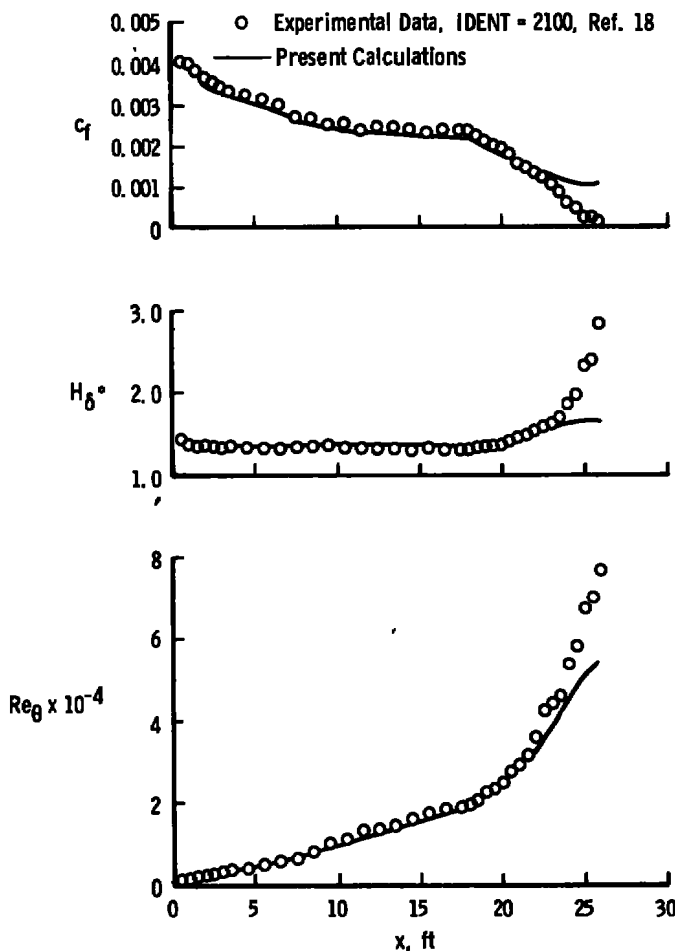


Figure 5. Present calculations and incompressible experimental measurements of Schubauer and Klebanoff (IDENT = 2100, Ref. 18).

However, those calculations shown in Ref. 2 which took three-dimensional flow effects into account were in better agreement with these experimental data than the present calculations. Three-dimensional effects were not considered in the present calculations. Comparisons of calculated and measured velocity profiles are shown in Fig. 6 for favorable, nearly zero, and severe adverse pressure gradient portions of the flow as indicated by the experimental values of β_{exp} . This agreement is considered good, even for the severe adverse pressure gradient at $x = 22.0$ ft.

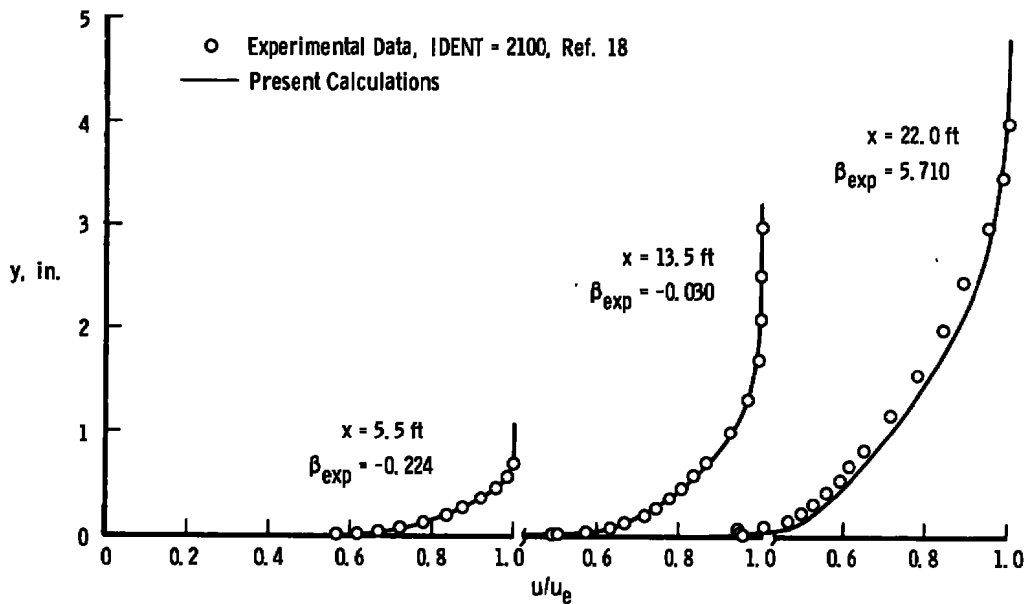


Figure 6. Favorable and adverse pressure gradient incompressible velocity profiles of Schubauer and Klebanoff (IDENT = 2100, Ref. 18).

In contrast to the experiment of Schubauer and Klebanoff (Ref. 18) where nearly all 27 calculation techniques (Ref. 2) were able to compute the flow with reasonable success, the experiment of Stratford (Ref. 18) had comparisons presented from only about half of these calculation techniques and of these only two succeeded in calculating reasonably good results for c_f , H_{δ^*} , and Re_{θ} (Ref. 2). Comparisons between the present calculations and the experiment of Stratford (Ref. 18) are given on Figs. 7 and 8. Of particular interest in these comparisons is the velocity profile in Fig. 8 for $\beta_{exp} = 78.988$ which appears to be extremely close to separation and yet the experimental velocity distribution is reasonably well calculated.

Boundary-layer measurements on an RAE 2822 airfoil in transonic flow have recently been made by Cook, McDonald, and Firmin (Ref. 19). Three sets of data from Ref. 19 are considered, and the pressure distributions are given in Fig. 9. Case 2

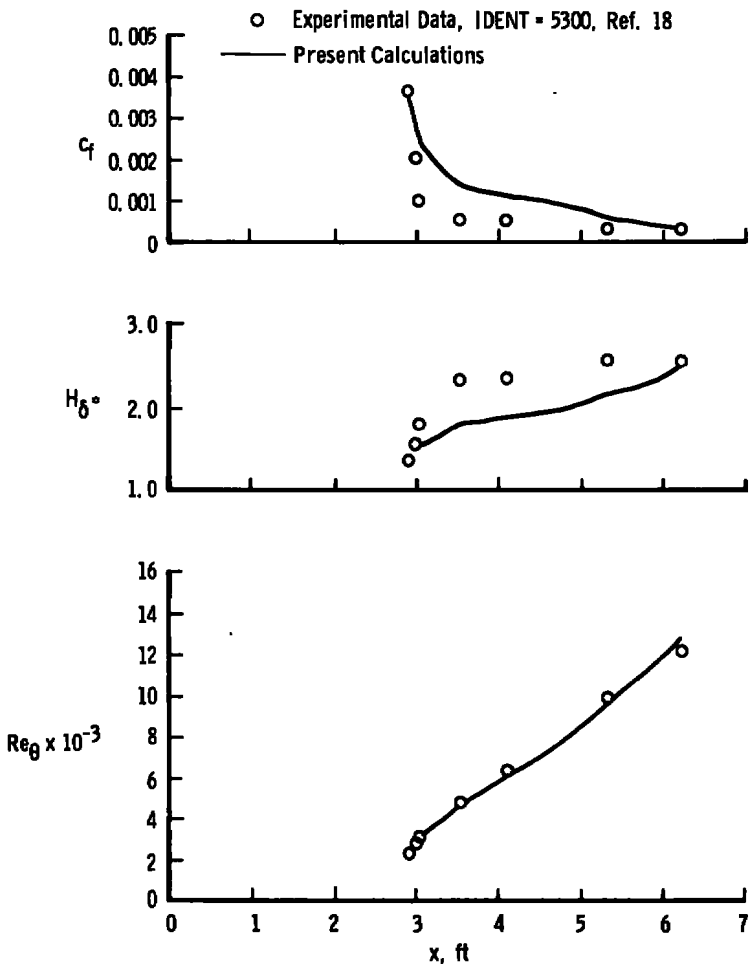


Figure 7. Present calculations and incompressible experimental measurements of Stratford (IDENT = 5300, Ref. 18).

represents a reasonably mild favorable and adverse pressure gradient flow where the flow is subcritical and the airfoil is at $\alpha = -2.18$ deg. Cases 9 and 12 represent commonly encountered supercritical flows with severe adverse pressure gradients caused by shocks on the airfoil ($\alpha = 3.19$ deg). Comparisons between calculated and measured values of c_f , δ^*/c , θ/c , and H_d^* are given in Fig. 10 for Case 2. These quantities vary smoothly along the airfoil and the agreement between calculations and measurements is good. Comparisons of the same quantities are made for Case 9 in Fig. 11. Good agreement is obtained up to the shock and reasonable agreement is obtained downstream of the shock. Case 12 was for the same conditions as Case 9 except the chord Reynolds number was reduced from 6.5×10^6 to 2.7×10^6 . Comparisons of calculated and measured data are presented in Fig. 12 for Case 12. The agreement in Fig. 12 is good except for the integral

quantities at $x/c = 0.9$. This experiment (Ref. 19) provides the opportunity to investigate the shock/boundary-layer interaction region in some detail. The three velocity profiles nearest the interaction (which are located just upstream, essentially at, and just downstream of the interaction) for Cases 9 and 12 are compared with the calculations in Figs. 13 and 14. The agreement in Fig. 13 for the higher $Re_{\infty,c}$ flow with an abrupt change in boundary-layer properties (see, e.g., the c_f distribution in Fig. 11 which illustrates this abrupt change) is considered reasonably good. The agreement in Fig. 14 is considered good with only a slight discrepancy between theory and experiment for the velocity profile in the interaction region at $x/c = 0.498$.

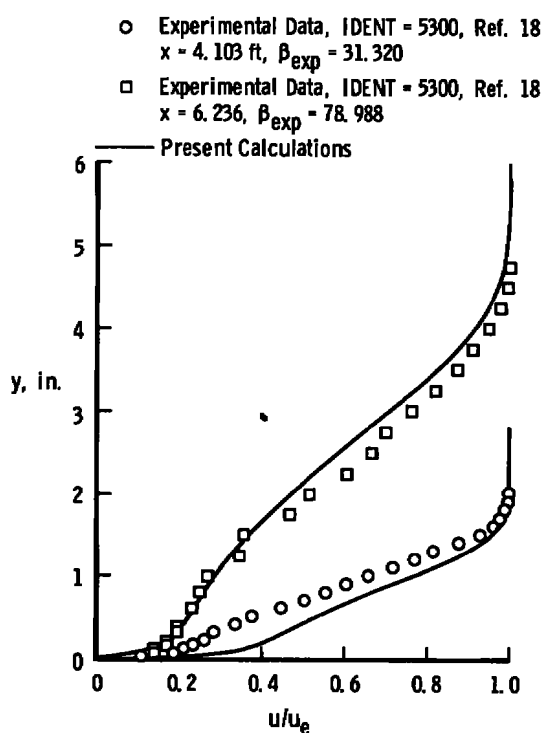


Figure 8. Severe adverse pressure gradient incompressible velocity profiles of Stratford (IDENT = 5300, Ref. 18).

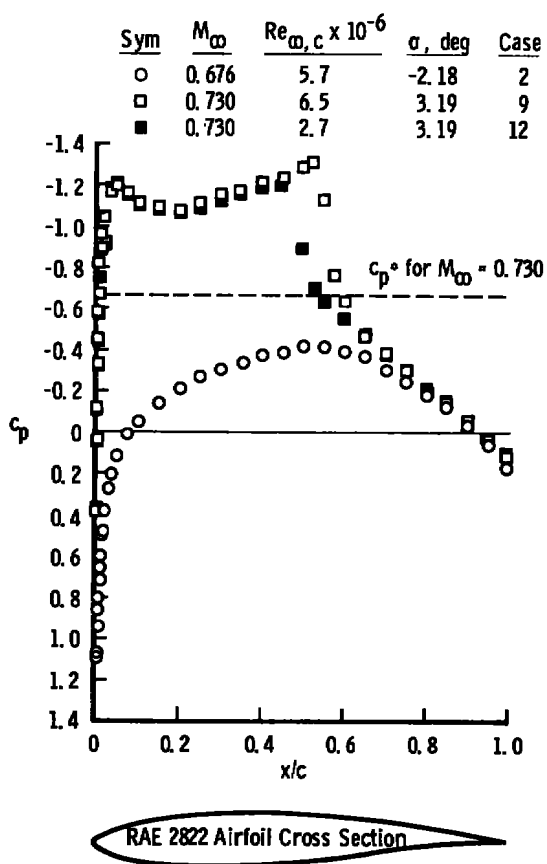


Figure 9. Upper surface pressure distributions on the RAE 2822 airfoil for Cases 2, 9, and 12 of Ref. 19.

Measurements by Pasiuk, Hastings, and Chatham (Ref. 20) were made for a compressible turbulent adiabatic wall boundary layer with a favorable pressure gradient.

Boundary-layer displacement and momentum thickness measurements are compared to present calculations in Fig. 15 and the agreement is considered good. The boundary-layer edge Mach number varied from about 1.5 to 3.0 for the data shown in Fig. 15.

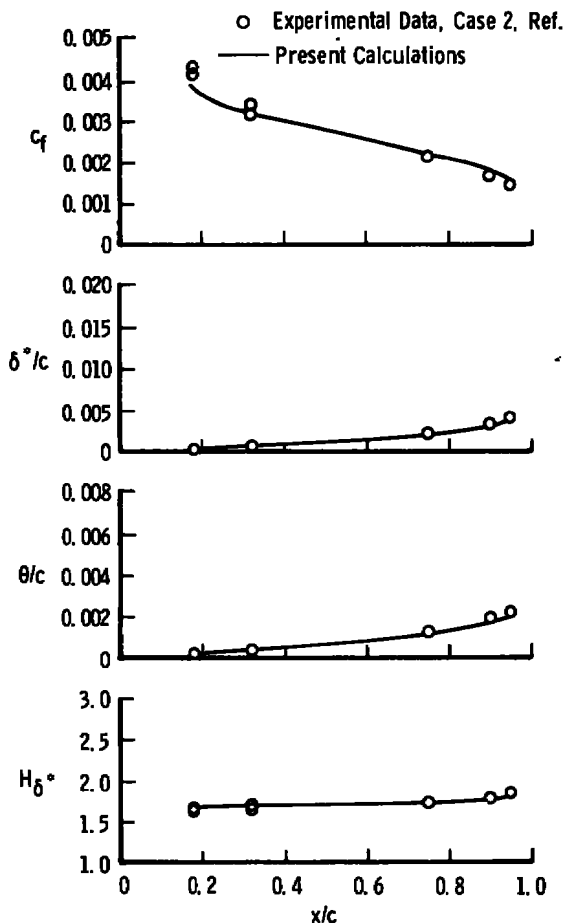


Figure 10. Upper surface boundary-layer properties of the RAE 2822 airfoil for $M_{\infty} = 0.676$, $Re_{\infty,c} = 5.7 \times 10^6$, and $\alpha = -2.18$ deg (Case 2).

An experimental investigation was performed by Winter, Rotta, and Smith (Ref. 21) on a waisted body of revolution in both subsonic and supersonic flow. Two sets of data from Ref. 21 are considered, $M_{\infty} = 0.597$, $Re_{\infty,\ell} = 9.98 \times 10^6$ and $M_{\infty} = 1.398$, $Re_{\infty,\ell} = 10.08 \times 10^6$. The pressure distributions for these two cases and the body geometry are shown in Fig. 16. Boundary-layer properties of c_f , δ^* , θ , and H_{δ^*} are compared with present calculations in Fig. 17 for $M_{\infty} = 0.597$ and in Fig. 18 for $M_{\infty} = 1.398$. The

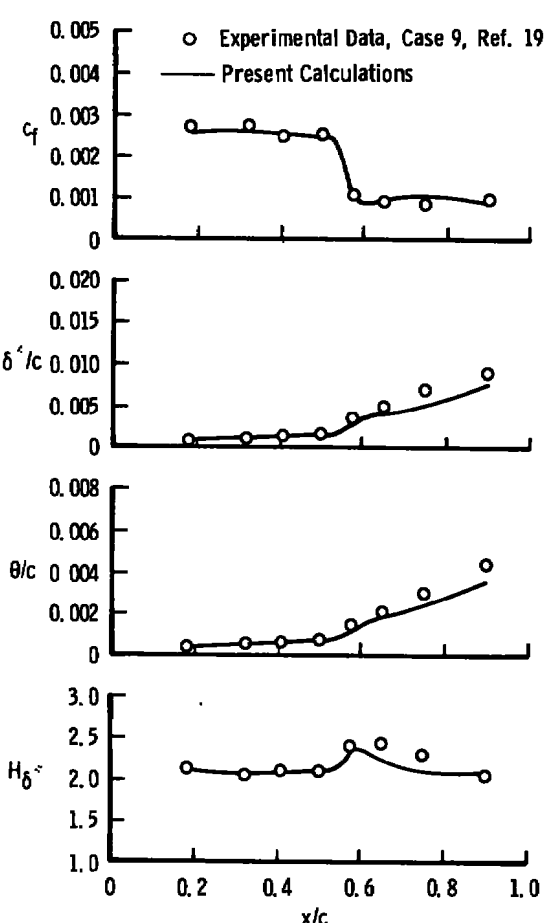


Figure 11. Upper surface boundary-layer properties of the RAE 2822 airfoil for $M_{\infty} = 0.730$, $Re_{\infty,c} = 6.5 \times 10^6$, and $\alpha = 3.19$ deg (Case 9).

calculated c_f is a little larger than the experiment for the $M_\infty = 0.597$ data, but the overall agreement in Fig. 17 is considered good. The agreement with the $M_\infty = 1.398$ data in Fig. 18 is good up to $x = 42$ in., but not as good over the remaining aft end of the body. In this connection, a compatibility check of the experimental data was performed by Winter, Rotta, and Smith (Ref. 21) by using measured values of c_f and H_{δ^*} in the momentum equation. The conclusion drawn in Ref. 21 from this exercise was that for the $M_\infty = 1.398$ data, the skin friction measurements appear to be too large for $x > 42$ in. This was attributed in Ref. 21 to the technique used to measure skin friction (the razor blade technique) which had not been completely established for these types of flow.

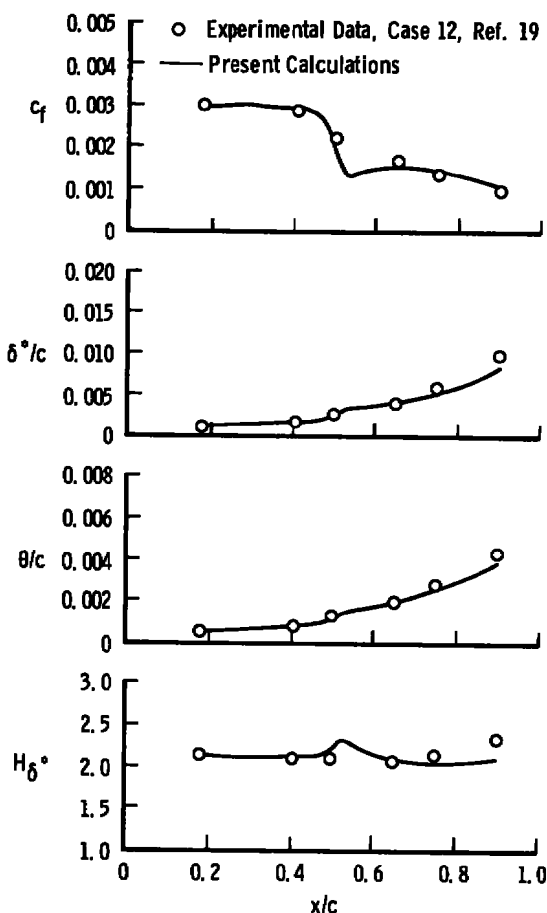


Figure 12. Upper surface boundary-layer properties of the RAE 2822 airfoil for $M_\infty = 0.730$, $Re_{\infty,c} = 2.7 \times 10^6$, and $\alpha = 3.19$ deg (Case 12).

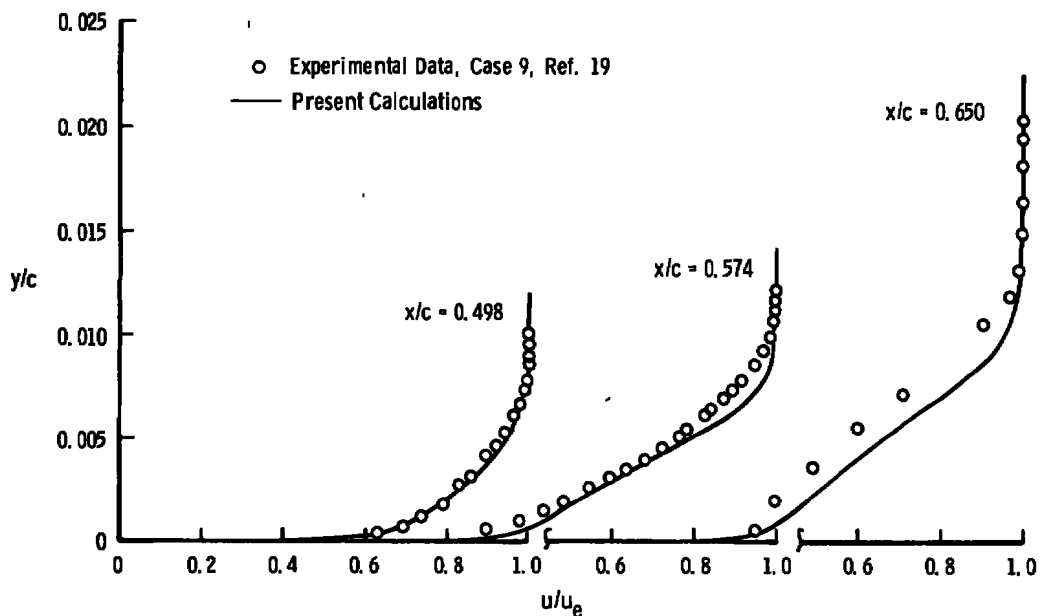


Figure 13. Velocity profiles in the shock region of the RAE 2822 airfoil for $M_\infty = 0.730$, $Re_{\infty,c} = 6.5 \times 10^6$, and $\alpha = 3.19$ deg (Case 9).

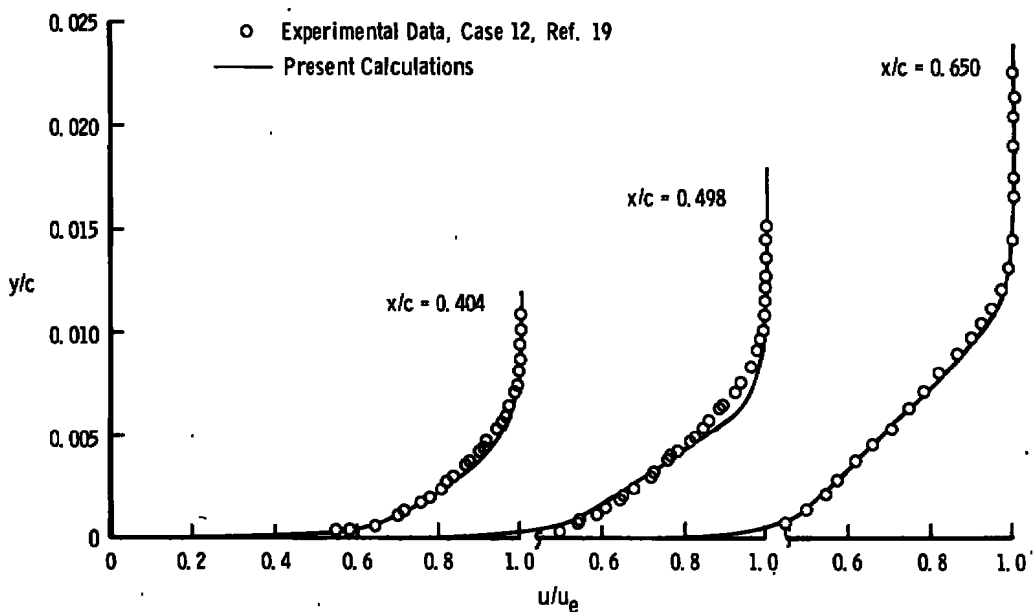


Figure 14. Velocity profiles in the shock region of the RAE 2822 airfoil for $M_\infty = 0.730$, $Re_{\infty,c} = 2.7 \times 10^6$, and $\alpha = 3.19$ deg (Case 12).

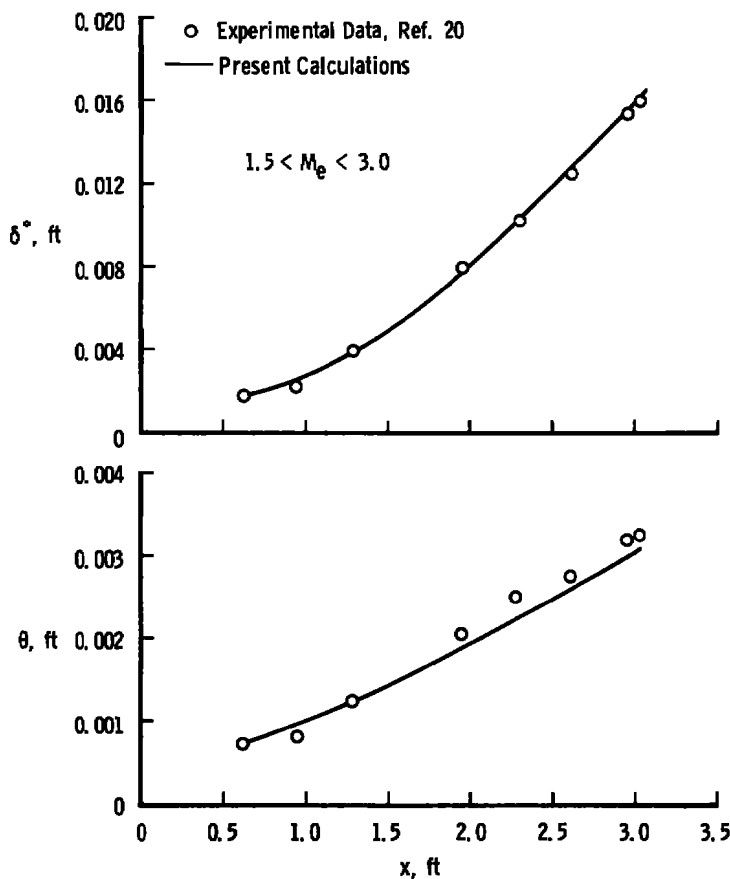


Figure 15. Boundary-layer displacement and momentum thickness distributions for a compressible adiabatic wall boundary layer with a favorable pressure gradient.

Velocity profiles for these two sets of data from Ref. 21 are compared with present calculations in Figs. 19 and 20. The agreement is good except for the last two downstream profiles in Fig. 20 which is poor. This is the same region of discrepancy as in Fig. 18. Also shown in Figs. 19 and 20 are the ratios of δ^*/r_w which must be small (i.e., $\delta^*/r_w \ll 1$) for transverse curvature to be unimportant (recall that this method is axisymmetric but does not account for transverse curvature). Note that regions of any significant discrepancies in Figs. 19 and 20 (excluding the last two downstream profiles in Fig. 20) occur near the outer edge of the boundary layers. It was pointed out in Ref. 6, where the velocity profile used here was developed, that the correlation for u/u_e at $y/\bar{\theta} = 5$ should be modified for axisymmetric flow. Therefore, the strictly two-dimensional planar correlation at $y/\bar{\theta} = 5$ is identified as the source of this discrepancy in Figs. 19

and 20. It should be pointed out, however, that the portion of the boundary layer for $y/\bar{\theta} < 5$ is the important part for the calculation of the shear-work integral term, Eq. (31).

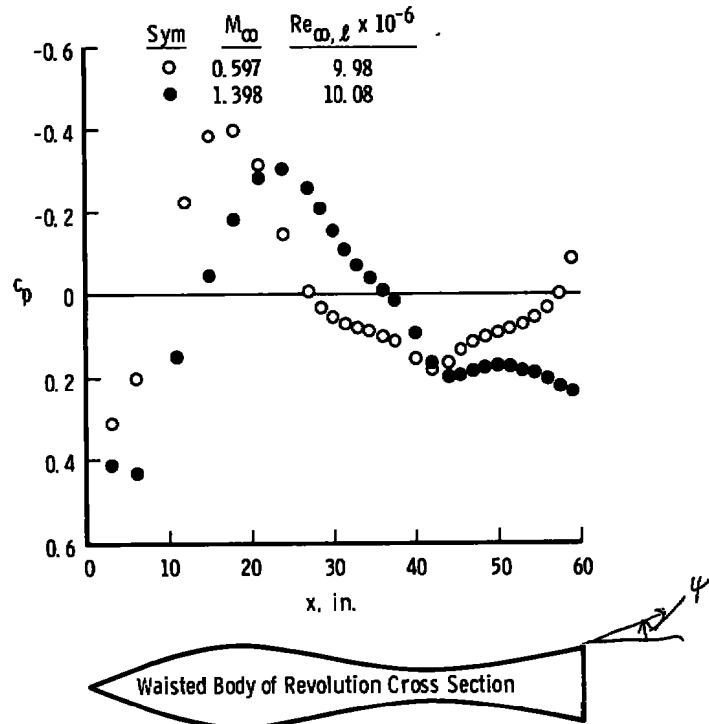


Figure 16. Pressure distributions on the waisted body of revolution for $M_\infty = 0.597$, $Re_{\infty, \ell} = 9.98 \times 10^6$ and $M_\infty = 1.398$, $Re_{\infty, \ell} = 10.08 \times 10^6$ (Ref. 21).

The most upstream boundary-layer profile measurements reported in Ref. 21 were at $x = 24$ in. Initial conditions near the nose were not available. This is usually the case in practice; therefore, it is of interest to investigate the influence of initial conditions on the solutions. Skin friction measurements were reported for $x < 24$ in. in Ref. 21 and these measurements provide an indication of the results that might be expected. Solutions for four sets of initial conditions are compared to these skin friction data for $M_\infty = 0.597$ and $Re_{\infty, \ell} = 9.98 \times 10^6$ (Ref. 21) in Fig. 21. Three solutions are for initial conditions at $x = 3$ in. and one for initial conditions at $x = 24$ in., which is the same solution as given in Fig. 17. As illustrated in Fig. 21, the three solutions beginning at $x = 3$ in. quickly

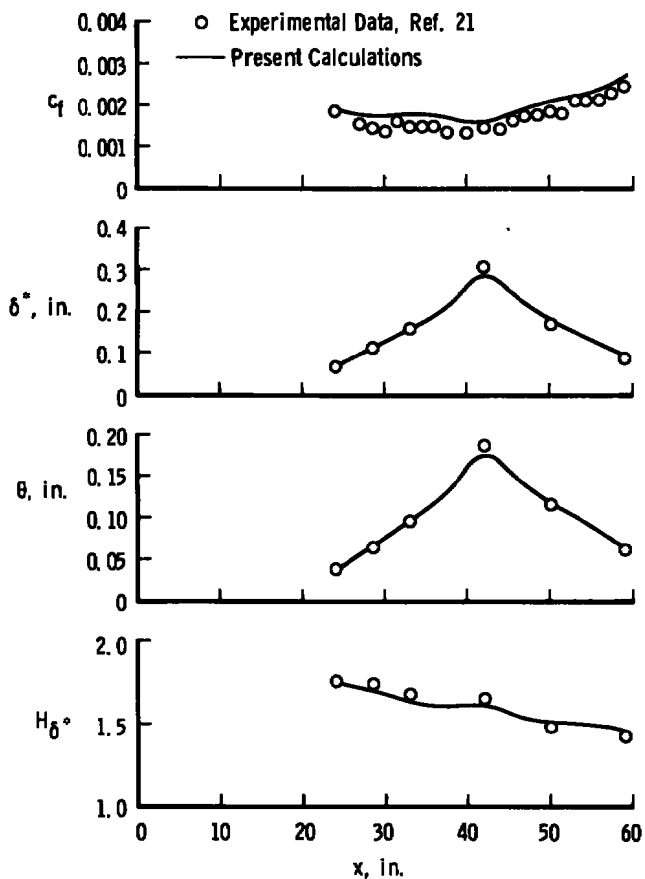


Figure 17. Boundary-layer properties on the waisted body of revolution for $M_\infty = 0.597$ and $Re_\infty \ell = 9.98 \times 10^6$.

converge to the same axial distribution of c_f . The solution beginning at $x = 24$ in. also has the same distribution, and converges to the same solution as the three solutions started at $x = 3$ in.

The data of Winter, Rotta, and Smith (Ref. 21) were used for comparisons with other calculation techniques. Blake (Ref. 22) compared these data with the finite difference calculation methods of Cebeci and Smith (Ref. 5), Harris (Ref. 23), and Blake (Ref. 22). Three figures were taken from Ref. 22 and included here along with the present calculations as Figs. 22, 23, and 24. It is important to note that these figures were copied from Ref. 22 because the plotted experimental data points differ somewhat from supposedly the same data ($M_\infty = 1.398$ and $Re_\infty \ell = 10.08 \times 10^6$) already used in Figs. 18 and 20. The discrepancies are not large, however, and direct comparisons of the

calculation methods can be made. Skin friction comparisons in Fig. 22 indicate that the present solution is close to Blake's solution (Ref. 22) up to about $x/\ell = 0.7$ and then is below the other solutions for $x/\ell > 0.7$ and below the experimental data for $x/\ell > 0.8$. As pointed out previously, however, it was concluded by Winter, Rotta, and Smith (Ref. 21) that the experimental skin friction appears too large over the aft portion of the body. Momentum thickness comparisons in Fig. 23 indicate that the present solution is essentially the same as Cebeci and Smith (Ref. 5) up to the maximum value of θ/ℓ , and then is between the Cebeci and Smith solution and Blake's and Harris' solutions (the two latter solutions are essentially the same) over the remaining aft end of the body. From the velocity distribution comparisons in Fig. 24 the present solution is considered to provide a better description of the experimental velocity profile than Blake's solution (Ref. 22). Velocity distributions from Cebeci and Smith (Ref. 5) and Harris (Ref. 23)

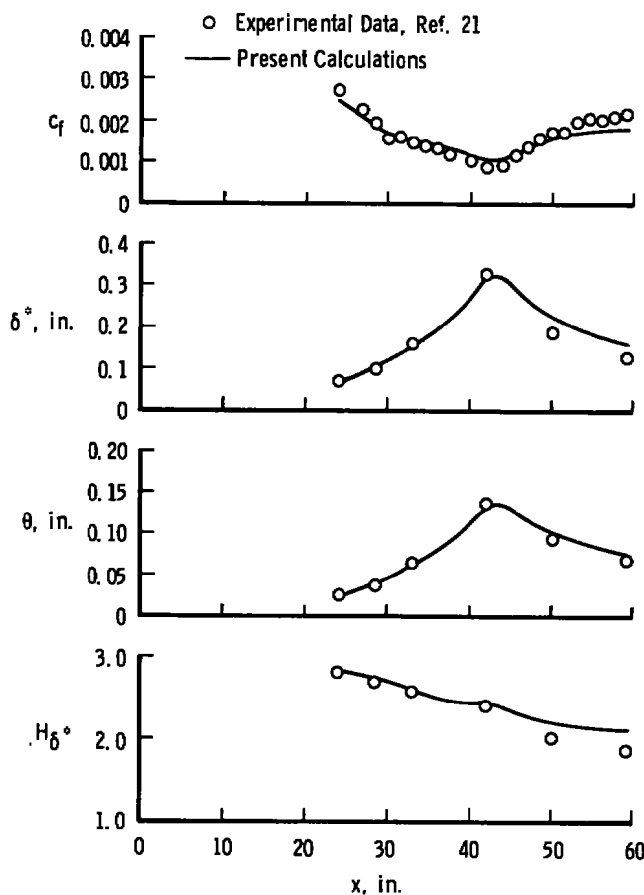


Figure 18. Boundary-layer properties on the waisted body of revolution for $M_\infty = 1.398$ and $Re_{\infty, \ell} = 10.08 \times 10^6$.

calculation methods were not given in Ref. 22. The discrepancy between experimental data and the present solution near the outer edge of the boundary layer was discussed above and attributed to neglecting transverse curvature. However, the slight inflection in the experimental velocity profile in Fig. 24 is well represented by the present integral solution, whereas the finite difference solution of Blake does not properly describe this feature of the boundary layer.

The experimental data of Winter, Rotta, and Smith (Ref. 21) were also considered by Lewis, Kubota, and Webb (Ref. 9) in their work concerning the application of transformation theory to turbulent boundary layers and the extension of Coles' (Ref. 8) analysis to include pressure gradient. The agreement obtained in Ref. 9 is considerably worse than the agreement obtained here with the same experimental data. Two possible sources of discrepancy are given in Ref. 9 as having to do with the low-speed formulation part of their transformation theory and/or the Mangler transformation which they used. Such problems are avoided by the present approach.

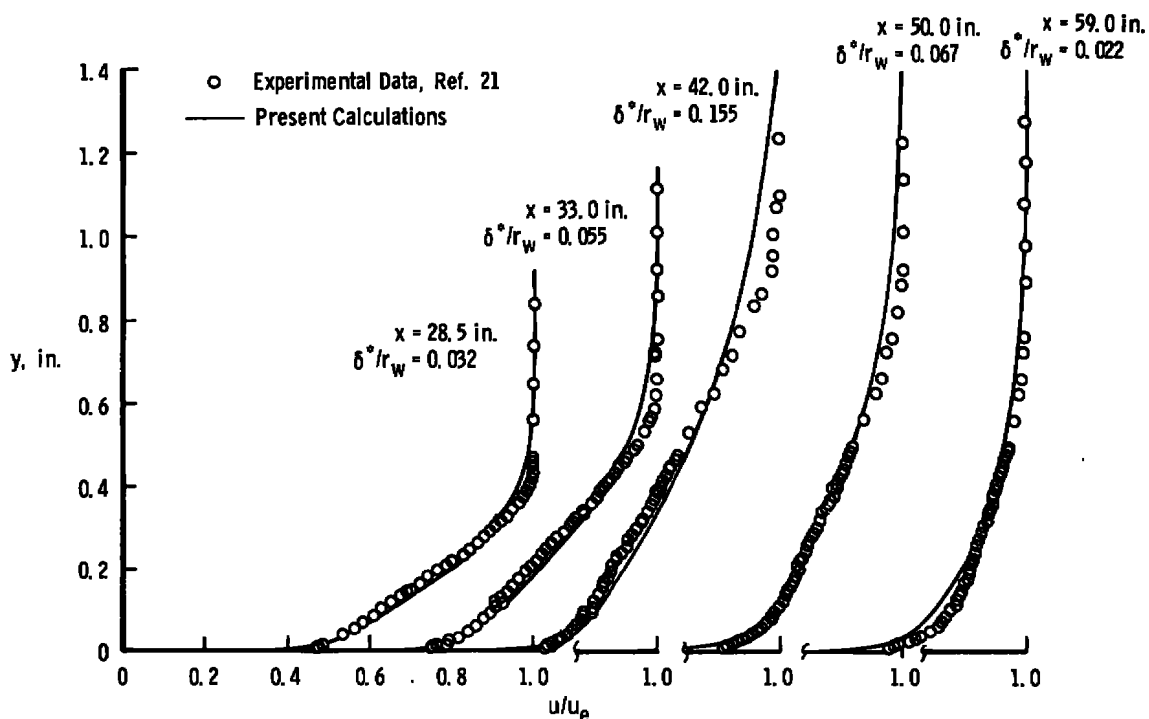


Figure 19. Velocity profiles on the waisted body of revolution for $M_\infty = 0.597$ and $Re_{\infty, \ell} = 9.98 \times 10^6$.

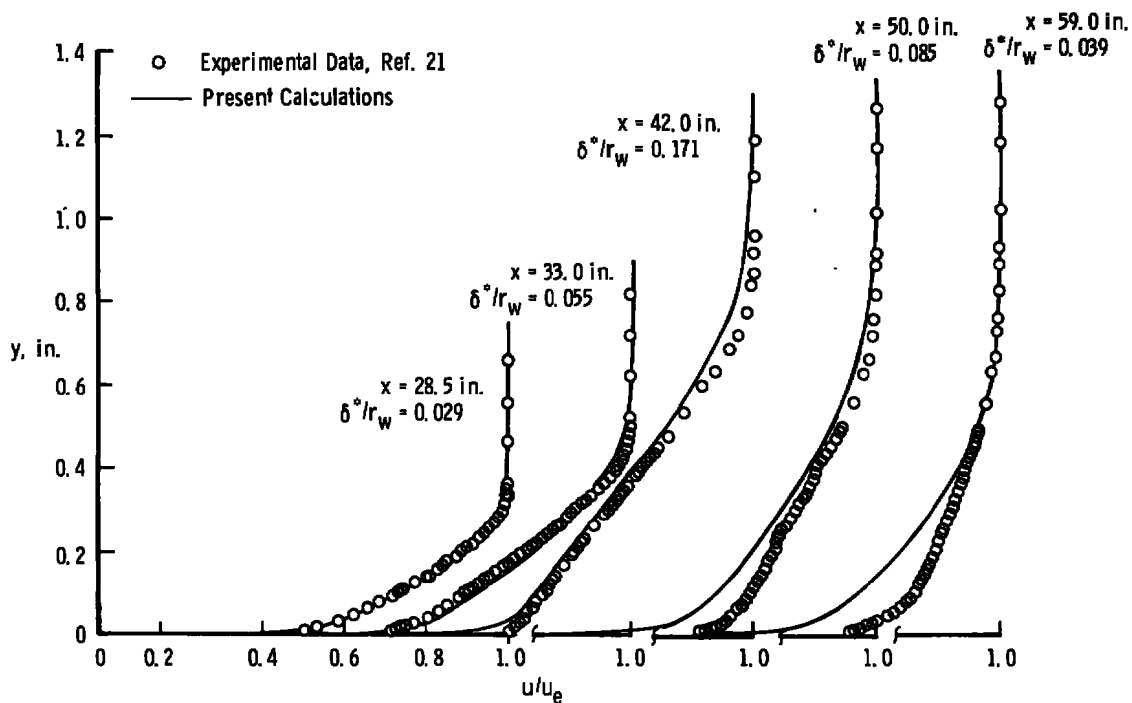


Figure 20. Velocity profiles on the waisted body of revolution for $M_\infty = 1.398$ and $Re_{\infty, \ell} = 10.08 \times 10^6$.

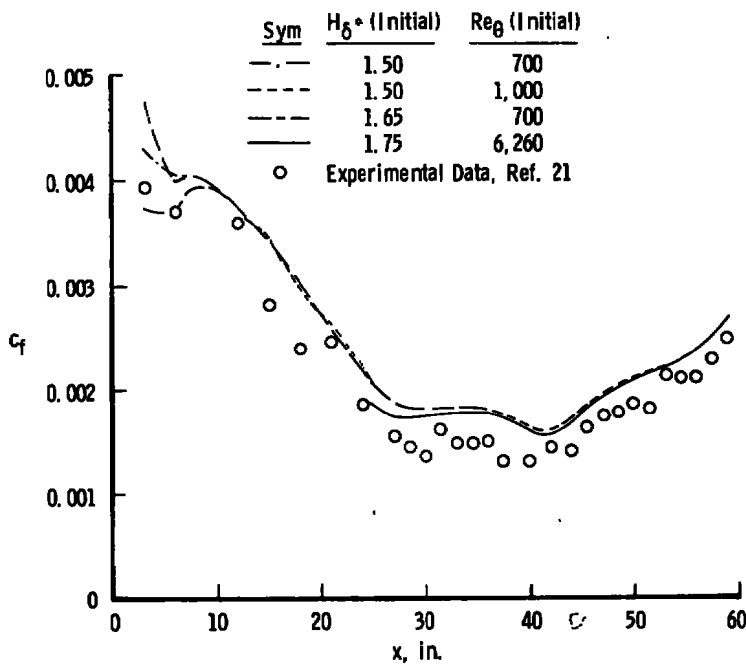


Figure 21. Influence of initial conditions on the waisted body of revolution for $M_\infty = 0.597$ and $Re_{\infty, \ell} = 9.98 \times 10^6$.

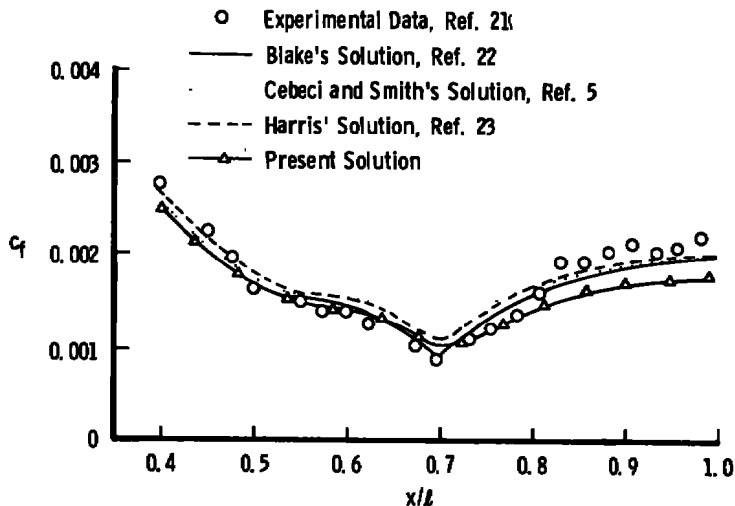


Figure 22. Calculated and measured skin friction distributions on the waisted body of revolution for $M_\infty = 1.398$ and $Re_{\infty, \ell} = 10.08 \times 10^6$.

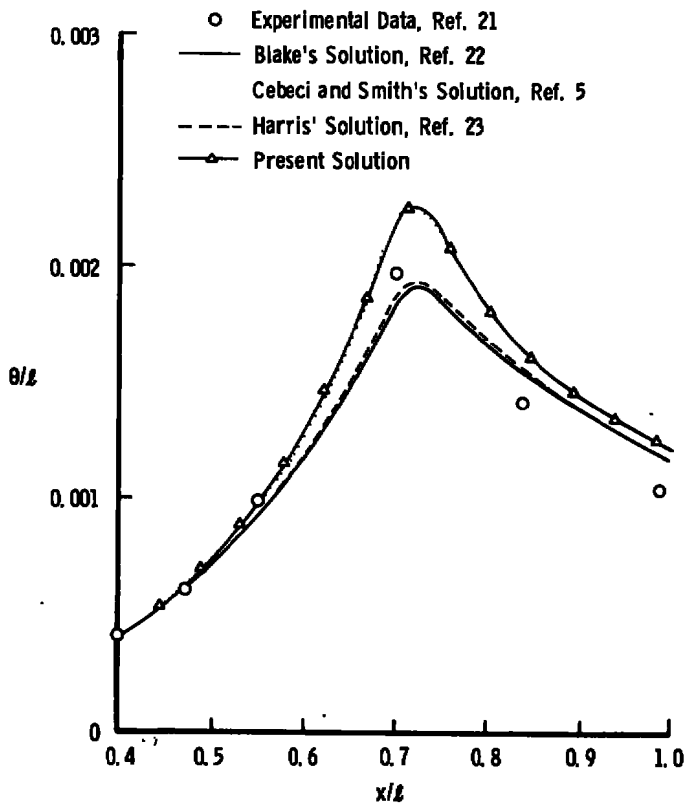


Figure 23. Calculated and measured momentum thickness distributions on the waisted body of revolution for $M_\infty = 1.398$ and $Re_{\infty, \ell} = 10.08 \times 10^6$.

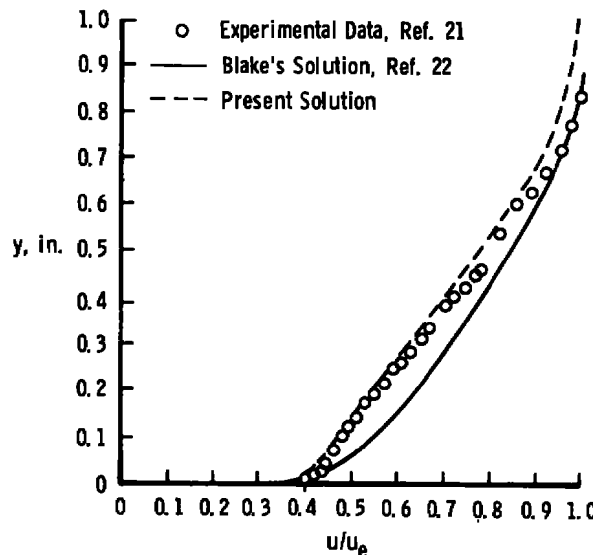


Figure 24. Calculated and measured velocity distributions on the waisted body of revolution for $M_\infty = 1.398$ and $Re_{\infty, \ell} = 10.08 \times 10^6$ at $x = 42$ in.

4.0 CONCLUSIONS

The objective of the present work was the development of a reasonably accurate and rapid means of calculating compressible turbulent adiabatic wall boundary layers on planar and axisymmetric bodies. Reasonably accurate solutions were obtained for the type of boundary-layer problems frequently encountered in PWT as illustrated by comparisons with transonic turbulent boundary-layer data. For the few direct comparisons afforded by the results in Blake's thesis (Ref. 22), the present integral method provided reasonable agreement with the finite difference methods of Cebeci and Smith (Ref. 5), Blake (Ref. 22), and Harris (Ref. 23). The present method is simple to use and about 42 x-steps can be solved per second on an IBM 370/165. The method no doubt could be improved, but the objective of the present work is considered satisfied.

The present approach differs from most integral approaches in three primary respects. First, an entirely different velocity profile (Ref. 6) was used. Second, the shear-work integral term was not correlated from experimental data, rather it was obtained by direct integration. And third, a new relation between velocity and temperature was used for shape factor calculations (Ref. 14), which accounted for total-temperature overshoot near the outer edge of turbulent boundary layers for the realistic conditions of nonunity Prandtl number and nonunity recovery factor.

REFERENCES

1. Bradshaw, P., Editor. Turbulence Topics in Applied Physics Vol. 12. Springer-Verlag Berlin Heidelberg, New York, 1976. Chapter 5.
2. Kline, S. J., Morkovin, M. V., Sovran, G., and Cockrell, D. S., Editors. Proceedings, Computation of Turbulent Boundary Layers - AFOSR-IFP-Stanford Conference. Vol. I. Stanford University Press, Stanford, California, 1968.
3. White F. M. Viscous Fluid Flow. McGraw-Hill Book Company, Inc., New York, N. Y., 1974.
4. Nash, J. F. "A Practical Calculation Method for Compressible Turbulent Boundary Layers in Two-Dimensional and Axisymmetric Flows." Lockheed-Georgia Company, Research Memorandum-ER-9428, August 1967.
5. Cebeci, T. and Smith, A.M.O. Analysis of Turbulent Boundary Layers. Academic Press, New York, N. Y., 1974.
6. Whitfield, D. L. "Analytical Description of the Complete Two-Dimensional Turbulent Boundary-Layer Velocity Profile." AEDC-TR-77-79 (ADA045033), September 1977. (Also AIAA Paper No. 78-1158, July 1978.)
7. Probstein, R. F. and Elliott, D. "The Transverse Curvature Effect in Compressible Axially Symmetric Laminar Boundary-Layer Flow." Journal of the Aeronautical Sciences, Vol. 23, No. 3, 1956, pp. 208-224, Concluded on p. 236.
8. Coles, D. E. "The Turbulent Boundary Layer in a Compressible Fluid." R-403-PR (AD285651), Rand Corporation, Santa Monta, California, September 1962.
9. Lewis, J. E., Kubota, T., and Webb, W. H. "Transformation Theory for the Adiabatic Compressible Turbulent Boundary Layer with Pressure Gradient." AIAA Journal, Vol. 8, No. 9, September 1970, pp. 1644-1650.
10. Winter, K. G. and Gaudet, L. "Turbulent Boundary-Layer Studies at High Reynolds Numbers at Mach Numbers Between 0.2 and 2.8." Aeronautical Research Council, London, R&M No. 3712, December 1970.
11. Coles, D. "The Law of the Wake in the Turbulent Boundary Layer." Journal of Fluid Mechanics, Vol. 1, 1956, pp. 191-226.
12. Hinze, J. O. Turbulence. Second Edition, McGraw-Hill, Inc., New York, 1975.

13. Clauser, F. H. "The Turbulent Boundary Layer." Advances in Applied Mechanics, Vol. 4, New York, 1956, pp. 1-51.
14. Whitfield, D. L. and High, M. D. "Velocity-Temperature Relations in Turbulent Boundary Layers with Nonunity Prandtl Numbers." AIAA Journal, Vol. 15, No. 3, March 1977, pp. 431-434.
15. Crocco, L. "Sulla Transmissione del Calore da una Lamina piana a un fluido Scorrente ad alta Velocita." L'Aerotechnica, Vol. XII, No. 2, February 1932, pp. 181-197. (Transmission of Heat from a Flat Plate to a Fluid Flowing at a High Velocity, NACA TM-690, October 1932.)
16. van Driest, E. R. "The Turbulent Boundary Layer with Variable Prandtl Number." in 50 Jahre Grenzschichtforschung, Friedr. Vieweg & Sohn, Braunschweig, 1955, pp. 257-271.
17. Whitfield, D. L. "Analytical, Numerical, and Experimental Results on Turbulent Boundary Layers." AEDC-TR-76-62 (ADA027588), July 1976.
18. Coles, D. E. and Hirst, E. A., Editors. Proceedings, Computation of Turbulent Boundary Layers - 1968 AFOSR-IFP-Stanford Conference. Vol. II, Stanford University Press, Stanford, California, 1968.
19. Cook, P. H., McDonald, M. A., and Firmin, M.C.P. "Aerofoil RAE 2822 - Pressure Distributions, Boundary Layer and Wake Measurements." Royal Aircraft Establishment. UK, AGARD WG O4, July 1977.
20. Pasiuk, L., Hastings, S. M., and Chatham, R. "Experimental Reynolds Analogy Factor for a Compressible Turbulent Boundary Layer with a Pressure Gradient." U. S. Naval Ordnance Laboratory, NOL TR-64-200, November 1964.
21. Winter, K. G., Rotta, J. C., and Smith, K. G. "Studies of the Turbulent Boundary Layer on a Waisted Body of Revolution in Subsonic and Supersonic Flow." Aeronautical Research Council 30935, Reports and Memoranda No. 3633, August 1968.
22. Blake, C. R. "Numerical Solution of the Compressible Boundary Layer Equations over Axisymmetric Surfaces." Master's Thesis, Air Force Institute of Technology Air University, GA/MC/76D-4 (ADA034943), December 1976.
23. Harris, J. E. "Numerical Solution of the Equations for Compressible Laminar, Transitional, and Turbulent Boundary Layers and Comparisons with Experimental Data." NASA TR R-368, August 1971.

APPENDIX A
LISTING OF THE BOUNDARY-LAYER COMPUTER CODE

FORTRAN IV G LEVEL 21

MAIN

```

0001      REAL M,MINF,MM(300),MOM(2),KE(2),M2
0002      DIMENSION X(2), XX(300),RR(300)
0003      2 FORMAT(1P11E12.4)
0004      3 FORMAT(8F10.5)
0005      4 FORMAT(I3)
0006      6 FORMAT(//,3X,'MACH NO. =',F6.3,5X,'UNIT REYNOLDS NO. =',F7.4,', MI
1LLION',//)
0007      7 FORMAT(1H1,5X,'X',11X,'R',11X,'H',9X,'THETA',9X,'H',11X,'CF',9X,
1 'DSTAR',7X,'BETA',9X,'REQ', 9X,'REX',8X,'DISS')
0008      8 FORMAT(' INPUT VALUES ARE',//6X,'XX',7X,'MM',8X,'RR',//)
0009      9 FORMAT(3F10.5)
0010      12 READ(5,3)MINF,REN,THETA,M
0011      READ(5,4) NINP
0012      READ(5,9) (XX(I),MM(I),RR(I),I=1,NINP)
0013      WRITE(6,8)
0014      WRITE(6,9) (XX(I),MM(I),RR(I),I=1,NINP)
0015      WRITE(6,6)MINF,REN
0016      X(1)=XX(1)
0017      I=0
0018      IPRINT=0
0019      500 KKK=0
0020      WRITE(6,7)
0021      1002 CONTINUE
0022      IF(I.LT.2) I=I+1
0023      IF(I-1)22,22,18
0024      18 DX=(XX(NINP)-XX(1))/500.
0025      20 X(I)=X(I-1)+DX
0026      IF((X(I)+DX-XX(NINP)).GE.0.0) IPRINT=1
0027      IF((X(I)-XX(NINP))22,22,120
0028      22 CONTINUE
0029      CALL LININT(X(I),XX,MM,M,DXM)
0030      CALL LININT(X(I),XX,RR,RAD,DUM)
0031      M2=M*M
0032      T=(1.+0.2*MINF**2)/(1.+0.2*M**2)
0033      U=M/MINF*SQRT(T)
0034      DU=DXM/(M*(1.+0.2*M**2))
0035      FC=SQRT(1.+M*M/5.)
0036      Q=U**2*T**2,5*RAD
0037      RE=REN*1.0E+06*U*T**1.74
0038      HLI=1.
0039      IF(I-1)30,30,36
0040      30 MOM(1)=Q*THETA
0041      HI=(H=0.290*M2)/(1.+0.113*M2)
0042      KE(1)=MOM(1)*U*(2.-0.54*TANH(1.1*(HI-1.))+0.028*M2)/(1.+0.014*M2)
0043      REQ=RE*MOM(1)/Q/FC
0044      CF=0.3*EXP(-1.33*HI)/ ALOG10(REQ)**(1.74+0.31*HI)
0045      UPE=SQRT(2./CF)
0046      CALL TURB(M2,UPE,REQ,HI,THETA,IPRINT,D)
0047      36 DO 60 K=1,6
0048      IF(I-1)42,42,40
0049      40 MOM(I)=MOM(I-1)+0.5*(DM+DMM)*DX
0050      KE(I)=KE(I-1)+0.5*(DK+DKK)*DX
0051      Z=(2.-KE(I)/MOM(I)/U)*(1.+0.014*M2)/0.54
0052      HI=1.+0.5* ALOG((1.+Z)/(1.-Z))/1.1
0053      H=HI*(1.+0.113*M2)*0.290*M2
0054      42 CF=0.3*EXP(-1.33*HI)/ ALOG10(REQ*MOM(I)/Q/FC)**(1.74+0.31*HI)/FC

```

FORTRAN IV G LEVEL 21

MAIN

```

0055      46 DM=0.5*Q*CF-MOM(I)*H*DU
0056      DK=Q*U*CF*D-2.*MOM(I)*U*DU*(0.064/(HI-0.8)+0.251)*M2
0057      IF(I-1)70,70,49
0058      49 IF(ABS(1.-HLI/HI)-0.0005)70,70,50
0059      50 HLI=HI
0060      60 CONTINUE
0061      DX=0.5*DX
0062      GO TO 20
0063      70 DMM=DM
0064      DKK=DK
0065      THETA=MOM(I)/Q
0066      DSTAR =H*THETA
0067      BETA=-2.*DSTAR/CF*DU
0068      REQCOM=RE*THETA
0069      REX=RE*X(I)
0070      WRITE(6,2)X(I),RAD,M,THETA,H,CF,DSTAR,BETA,REQCOM,REX,D
0071      UPE=SQRT(2./(CF*FC))
0072      REQ=REQCOM/FC
0073      THETAI=THETA/(1.-0.92*M2/(7.09+M2)*TANH(1.49*(HI-0.9)))
0074      CALL TURB(M2,UPE,REQ,HI,THETAI,IPRINT,D)
0075      KKK=KKK+1
0076      IF(I.EQ.1) GO TO 1002
0077      X(1)=X(2)
0078      MOM(1)=MOM(2)
0079      KE(1)=KE(2)
0080      IF(KKK.EQ.57)GO TO 500
0081      GO TO 18
0082      120 CONTINUE
0083      STOP
0084      END

```

FORTRAN IV G LEVEL 21

LININT

```

0001      SUBROUTINE LININT(X,XX,YY,Y,DY)
0002      DIMENSION XX(300),YY(300)
0003      N=1
0004      1 N=N+1
0005      IF(X.GT.XX(N)) GO TO 1
0006      DY=(YY(N)-YY(N-1))/(XX(N)-XX(N-1))
0007      Y=YY(N-1)+(X-XX(N-1))*DY
0008      RETURN
0009      END

```

FORTRAN IV G LEVEL 21

TURB

```

0001      SUBROUTINE TURB(XM2,UPE,RET,H,THETA,IPRINT,D)
0002      DIMENSION F(101)
0003      PI=3.141592
0004      RETUP=RET/(UPE**2)
0005      REUP9=0.09*RET/UPE
0006      PIUPE=PI/(.18*UPE)
0007      UUE2=1.723*EXP(-0.6*H)*(1.+50./RET)
0008      UUE5=0.87+0.08*EXP(-2.6*(H-1.95)**2)
0009      G2=(UUE2-(1./(.09*UPE))*ATAN(2.*REUP9))/(1.-PIUPE)
0010      G5=(UUE5-(1./(.09*UPE))*ATAN(5.*REUP9))/(1.-PIUPE)
0011      B=ALOG((.5*ALOG((1.+G2**2)/(1.-G2**2)))/(.5*ALOG((1.+G5**2)/(1.-G5**2))))/ALOG(0.4)
0012      A=(.5*ALOG((1.+G2**2)/(1.-G2**2)))/2.**B
0013      N=101
0014      DX=10./100.
0015      SUM=0.
0016      X=UPE*100./RET-DX
0017      DO 9000 I=1,N
0018      X=X+DX
0019      Y=X*THETA
0020      YPLUS=X*RET/UPE
0021      ARG=A*X**B
0022      IF (ARG.GT.87.3) F(I)=0.
0023      IF (ARG.GT.87.3) GO TO 9000
0024      HCOS=(COSH(ARG))**2
0025      HTAN=SQRT(TANH(ARG))
0026      UPLUS=ATAN(REUP9*X)/0.09+(UPE-PI/0.18)*HTAN
0027      UUE=UPLUS/UPE
0028      F(I)=RETUP*(1./(1.+(REUP9*X)**2))+(1.-PIUPE)*ARG*B/2./X
0029      1*(1./(HTAN*HCOS))
0030      XL=0.41*X
0031      FFC=0.0168*H*F(I)
0032      FF=XL*XL*F(I)*F(I)
0033      IF (FF.GT.FFC) SUM=SUM+1.
0034      IF (SUM.GT.0.) FF=FFC
0035      F(I)=FF*F(I)/(1.+0.176*XM2*(1.-UUE*UUE))
0036      IF (IPRINT.EQ.1.AND.I.EQ.1) WRITE(6,10)
0037      10 FORMAT('1',5X,'Y', 8X,'Y/THETA1',7X,'Y+',10X,'U+', 9X,'U/UE')
0038      IF (IPRINT.EQ.1) WRITE(6,11) Y,X,YPLUS,UPLUS,UUE
0039      11 FORMAT(1P5E12.4)
0040      9000 CONTINUE
0041      CALL SIMP(F,F2,F4,N)
0042      CP=DX/3.*(F(1)+F2+F4+F(N))
0043      D=16.79/UPE*UPE*UPE*CP
0044      RETURN
      END

```

FORTRAN IV G LEVEL 21

SIMP

```

0001      SUBROUTINE SIMP(F,F2,F4,N)
0002      DIMENSION F(101)
0003      FODD=0.0
0004      FEVEN=0.0
0005      N1=N-1
0006      N2=N-2
0007      DO 30 I=3,N2,2
0008      30 FODD=FODD+F(I)
0009      F2=2.*FODD
0010      DO 40 I=2,N1,2
0011      40 FEVEN=FEVEN+F(I)
0012      F4=4.*FEVEN
0013      RETURN
0014      END

```

The following is an example set of input data for the Waisted Body of Revolution (Ref. 21) for $M_\infty = 0.597$ and $Re_\infty l = 9.98 \times 10^6$.

	.597	.1642	.0363	1.751
022				
24.0	.642	4.359		
27.0	.598	3.793		
28.5	.585	3.515		
30.0	.578	3.257		
31.5	.573	3.0199		
33.0	.569	2.7981		
34.5	.567	2.594		
36.0	.563	2.404		
37.5	.559	2.222		
40.0	.545	1.963		
42.0	.537	1.87		
44.0	.542	1.933		
45.5	.552	2.067		
47.0	.558	2.231		
48.5	.563	2.407		
50.0	.567	2.597		
51.5	.569	2.802		
53.0	.573	3.023		
54.5	.578	3.262		
56.0	.585	3.52		
57.5	.597	3.798		
59.0	.623	4.097		

NOMENCLATURE

a	Parameter used and defined in Table 1
b	Parameter used and defined in Table 1
c	Airfoil chord
c_f	Local skin friction coefficient, τ_w/q_e
c_p	Pressure coefficient, $(p-p_\infty)/q_\infty$
c_p^*	Critical pressure coefficient
D	Shear-work integral, defined by Eq. (26)
\tilde{D}	Defined by Eq. (19)
F_c	$(1 + 0.2 M_e^2)^{1/2}$
g	Function used and defined in Table 1
H	Specific total enthalpy
\bar{H}	$\bar{\delta}^*/\theta$
H_δ^*	δ^*/θ
H_δ^{**}	δ^{**}/θ
H_θ^*	θ^*/θ
k	Index which is zero for planar flow and one for axisymmetric flow
ℓ	Mixing length, $\ell = 0.41 y$; also total body length
M	Mach number
m	Index which is zero for the momentum integral equation and one for the mean-flow kinetic energy integral equation
Pr	Molecular Prandtl number
Pr_t	Turbulent Prandtl number

p	Static pressure
q	Dynamic pressure, $\rho u^2/2$
$Re\theta$	$\rho_e u_e \theta / \mu_e$
$Re_{\infty,c}$	$\rho_{\infty} u_{\infty} c / \mu_{\infty}$
$Re_{\infty,\ell}$	$\rho_{\infty} u_{\infty} \ell / \mu_{\infty}$
r	$r_w \pm y \cos \psi$; also used as recovery factor ($r = 0.88$)
r_w	Local body radius
T	Static temperature
u	Mean velocity in the x direction
u^+	u/u_{τ}
u_{τ}	$(\tau_w / \rho_w)^{1/2}$
v	Mean velocity in the y direction
x	Coordinate along the body surface
y	Coordinate normal to the body surface
y^+	$\rho_w u_{\tau} y / \mu_w$, $(\overline{Re\theta} / \overline{u_e})^+ (y / \overline{\theta})$
α	Angle of attack, deg
β	δ^* / τ_w dp/dx
δ^*	Boundary-layer displacement thickness defined by Eq. (23)
$\bar{\delta}^*$	Defined by Eq. (36)
$\tilde{\delta}^*$	Defined by Eq. (16)
δ^{**}	Defined by Eq. (25)
$\bar{\delta}^{**}$	Defined by Eq. (18)
ϵ	Eddy viscosity, defined by Eq. (32)
ϵ_m	Middle boundary-layer region eddy viscosity, defined by Eq. (33)

ϵ_0	Outer boundary-layer region eddy viscosity, defined by Eq. (35)
θ	Boundary-layer momentum thickness, defined by Eq. (22)
$\bar{\theta}$	Low-speed or kinematic boundary-layer momentum thickness, $\bar{\theta} = \int_0^\infty u/u_e dy$
$\tilde{\theta}$	Defined by Eq. (15)
θ^*	Defined by Eq. (24)
$\tilde{\theta}^*$	Defined by Eq. (17)
μ	Molecular viscosity
ρ	Density
$-\rho \bar{u}' \bar{v}'$	Reynolds stress
τ	Total shear stress, $(\mu + \rho \epsilon) \partial u / \partial y$
τ_t	Turbulent shear stress, $\rho \epsilon \partial u / \partial y$
ψ	Local body surface angle

SUBSCRIPTS

e	Boundary-layer edge value
exp	Experimental value
w	Wall value
∞	Free-stream value

SUPERSCRIPT

—	Denotes low-speed or incompressible value
---	---